Renewable Energy 184 (2022) 881–898

Contents lists available at ScienceDirect

Renewable Energy

journal homepage: www.elsevier.com/locate/renene

The energetic, exergetic, and mechanical comparison of two structurally optimized non-concentrating solar collectors for intermediate temperature applications

Datong Gao [a], Shuai Zhong [a], Xiao Ren [b], Trevor Hocksun Kwan [a], Gang Pei [a, *]

[a] Department of Thermal Science and Energy Engineering, University of Science and Technology of China, Hefei, 230027, China
[b] College of New Energy, China University of Petroleum (East China), Qingdao, 266580, China

ARTICLE INFO

Article history:
Received 24 August 2021
Received in revised form
3 December 2021
Accepted 5 December 2021
Available online 8 December 2021

Keywords:
Solar energy
Intermediate temperature
Solar collector
Exergy

ABSTRACT

The highly efficient non-concentrating solar collector is a key component for increasing solar energy penetration at the district level, thereby achieving the "carbon neutrality" goal. The non-concentrating vacuum-type solar collector used for intermediate temperature (100–200 °C) applications is a promising technology that has not been sufficiently explored. In this paper, two structurally optimized non-concentrating solar collectors have been meticulously analyzed from the perspective of structure, energy, exergy, surface stress, etc. Firstly, an outdoor experiment is executed to exhibit their thermodynamic behavior. Thermal resistance networks before and after their structural optimization are formed and the results indicate the thermal resistance that impedes solar collector heat loss has been enhanced by 3.83 and 4.17-fold, respectively. Next, energy and exergy flow charts are established to explain the thermal performance difference and the solar energy conversion in their respective internal components. Finally, the potential room for performance enhancement is further studied via the advanced exergy analysis method which reveals that the exergy destruction can be reduced by 17.74% and 13.90%, respectively. The results are essential for the further development of non-concentrating solar collectors in intermediate temperature applications, and it is also instrumental to realizing the decarbonization in district energy supplements.

1. Introduction

With the huge amount of fossil energy consumption, energy and environmental problems have become grimmer globally [1]. Many countries around the world have put forward a series of measures to achieve the goal of "carbon neutrality". Efficient use of renewable energy is a critical part of achieving this intention. Solar energy is a kind of renewable energy that is promising to be dominated in the future energy structure, and it has the advantages of being ubiquitous and inexhaustible [2].

Generally, solar energy is collected by solar collectors of two categories, i.e. concentration solar collectors (such as the solar tower collector [3] and parabolic trough solar collector [4]) and non-concentration solar collectors (such as flat plate solar collector [5] and evacuated tube solar collector [6]). The concentrating solar collectors are usually used in large-scale occasions for grid-level power generation [7], and the plant location is generally far from the users. Hence, it brings long-distance energy delivery and extra management cost-related problems. Besides, the concentrating solar collectors usually need tracking devices to obtain the maximum solar direct irradiance which leads to higher capital costs and insufficient utilization of solar diffuse irradiance energy [8].

In contrast, non-concentration solar collectors are usually used in intermediate or small-scale applications which makes it easier to be integrated with buildings [9] and more flexible in the district energy systems [10]. From the perspective of solar collectors' operating temperature grade, the solar collectors can be divided into low temperature (<100 °C), intermediate temperature (100–200 °C), and high temperature (>200 °C) types [11]. According to the second law of thermodynamics, a higher temperature grade allows more exergy obtained from solar energy [12]. However, the non-concentrating solar collector commonly works in the low-temperature range. In the intermediate temperature range, its thermal efficiency becomes very limited or even negative due to

* Corresponding author.
E-mail address: peigang@ustc.edu.cn (G. Pei).

https://doi.org/10.1016/j.renene.2021.12.025
0960-1481/

Nomenclature

Symbols

A	area, m^2
c_p	specific thermal capacity, J/(kg·K)
d	distance, m
E	exergy power, W
G	solar irradiance, W/m^2
h	specific enthalpy, J/kg
h_c	heat transfer coefficient, $W/m^2·K$
$\dot{m}$	mass flow rate, kg/s
Nu	Nusselt number
R	thermal resistance, $K·m^2/W$
Ra	Rayleigh number
s	specific entropy, J/kg·K
T	temperature, K
T_i*	normalized temperature difference, $K·m^2/W$

Abbreviations

EFPC	evacuated flat plate solar collector
ETSC	evacuated tube solar collector
HTF	heat transfer fluid
RE	relative error
RSMD	root mean square error

Subscripts

abs	absorber plate
ad	downside of absorber plate
amb	ambient
at	top side of absorber plate
bot	bottom
con	condensation section
conv	heat convention
d	exergy destruction
dst	exergy destroy
ex	exergy
exp	experiment
ga	glass aperture area
gla	glass
grd	ground
ht	heat absorb tube
i	inlet
ins	insulation
inv	interval
pc	condensation section of the heat pipe
pe	evaporation section of the heat pipe
r	heat radiation
s	sun
SF	solar field
shd	shield
sim	simulation
tre	trepanning
w	water

Superscripts

AVO	avoidable exergy destruction
hypo	hypothetical working condition
k	k_{th} component
real	real working condition
UN	unavoidable exergy destruction

Greek letters

α	absorptivity
ε	emissivity
η	efficiency
λ	heat conductivity coefficient
τ	transmittance
ψ	Petela coefficient

huge heat loss. As shown in Fig. 1, more applications can be realized at 100–200 °C, but the corresponding solar collector technologies are mostly the concentrating ones. The low-temperature energy output eliminates their competitiveness with solar photovoltaic panels [13]. Besides, it will impede the development for significant intermediate temperature demand in both industrial and domestic sectors [14]. For example, numerous district space heating projects adopt non-concentrating solar collectors for reducing fossil fuel energy consumption in the heating seasons. However, the lower heat demand in the non-heating seasons results in the solar collectors being idle for most time in the whole year [15]. If the non-concentrating solar collectors have better performance in the intermediate temperature range, they can make the most use of solar energy in the non-heating seasons with intermediate temperature applications, such as solar absorption chiller [16], industrial process heat [17], solar sterilization [18] and so on. Intermediate temperature applications with non-concentrating solar collectors will avoid the tracking device and make full use of solar beam and diffuse irradiance. Hence, many attempts have been conducted for elevating its temperature grade to broaden its application occasions [19].

The flat plate solar collector and evacuated tube solar collector are two kinds of non-concentrating solar collectors that have been applied very extensively. Some researchers use various structural improvement methodologies to enhance their heat transfer effectiveness. For example, nanofluids have been applied as a kind of heat transfer fluid that has better thermodynamic properties than water [21]. In another case study, the evacuated tube solar collector was improved by integrating a heat pipe technology that enhances the anti-freeze and corrosion-resistant characteristics [22]. Some other solutions are hammering at the heat absorber tubes, such as using porous metal foam [23] to enhance the heat transfer between heat transfer fluid and heat absorber tubes, low-ratio concentration structure [24], bilateral absorber plate [25] for heat pipe evacuated tube solar collector, and so on. For such a mass of evacuated tube types, the flat plate absorber is more promising in the practical application than others since its easy processing and relatively low costs.

Inert gases (such as Ar and Kr) are used for reducing the energy losses of flat plate solar collector since it has a low thermal conduction coefficient. When they are used for the flat plate solar collector instead of the air interlayer, the energy losses can be reduced by as much as 20% [26]. If decrease its pressure furtherly, the heat conduction effect can also be held back [27]. With implemented of the vacuum technology, a kind of evacuated flat plate solar collector is developed by Ref. [28], and a software simulation is used to analyze the stress distribution and to optimize the geometric dimension. Its performance is studied through a solar simulating light source [29], and an efficiency curve is obtained [30]. For practical application purposes, the evacuated flat plate collector and organic Rankine cycle are coupled to study its thermal characteristics and economic performance [31].

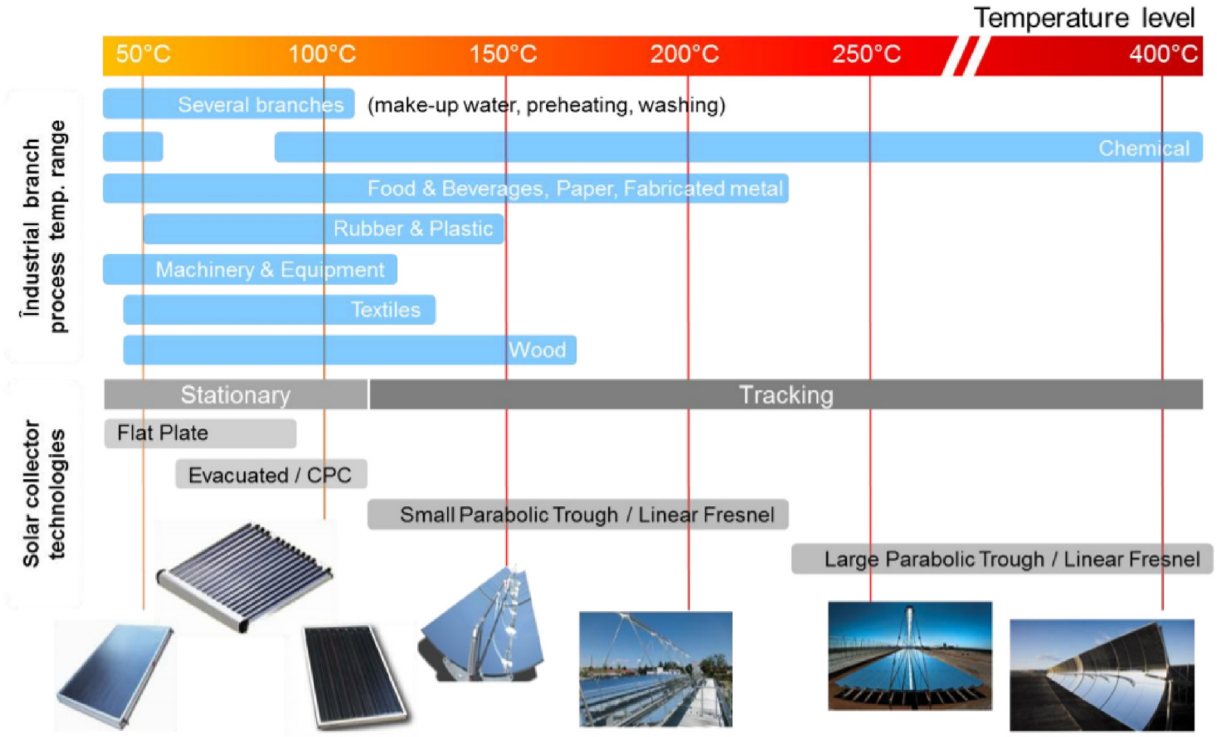

Fig. 1. The temperature range and application of different collectors [20].

Another potential candidate for non-concentrating solar thermal harvesting technology is optically transparent thermally insulating materials such as silica aerogel, which is transparent to solar irradiance and opaque to infrared radiation. For instance, the tetramethyl orthosilicate-based silica aerogel [32], graphene aerogel [33], plasmonic aerogel [34], and so forth have been applied for the non-concentrating solar collector in intermediate solar applications. In addition, energy transfer optimization should also be considered in the collector design process, Mosavati et al. [35] have proposed a new approach for obtaining desirable heat flux on the design surfaces, and its efficiency in the heat radiation optimization process is proved [36].

Some comparison works about non-concentrating solar collectors have also been conducted on the flat plate and evacuated tube solar collectors in terms of their energy performance under different regions [37] and applications [38,39]. Besides using water as heat transfer fluid, a comparison of their thermal performance using nanofluids has also been carried out [40]. Sokhansefat et al. evaluated the flat plate and evacuated tube solar collectors with a simple economic model [41]. In addition, the influence on the environment is accessed via life cycle assessment of flat plate and evacuated tube solar collectors [42].

For the above studies for the non-concentrating solar collectors, most of the literature only focuses upon the performance enhancement of a certain collector (mostly working in the relatively low temperature). As the technology advances, the non-concentrating vacuum-type solar collectors will be more prevalent for intermediate temperature applications. However, the knowledge gap of the internal energy and exergy transfer relationships among the components in the solar collectors, the essential structural improvement methods on the solar collectors, and the room for further enhancement of vacuum-type solar collectors have not been properly discussed and addressed. Specifically, two types of structurally optimized non-concentrating solar collectors, namely the heat pipe evacuated tube solar collector (ETSC) with a shield plate and the evacuated flat plate solar collector (EFPC), as two structure optimized non-concentrating solar collectors, have hardly ever been contrastively studied before. A shield plate is added to the ETSC that can eliminate the heat radiation loss from the bottom of the absorber plate. Hence, other than the heat resistance for heat conduction and convention by vacuum, the shield plate can also hold back the heat radiation loss on the bottom side of the absorber plate. In addition, a high-performance flat plate solar collector is developed with a vacuum environment, which can also greatly eliminate heat loss. This kind of novel evacuated flat plate solar collector can not only improve the thermal insulation performance of the ordinary flat plate solar collector, but it can also make full use of the floor space since there is no tube gap like the evacuated tube solar collector.

To make an elaborate comparison of these two structurally optimized non-concentrating solar collectors and solve the above knowledge gaps, the outdoor experiment test and numerical model are conducted for both of them. Detailed energy flow and exergy destruction analyzes are also carried out for their distinct structures, which aims to demonstrate the effectiveness of structural optimization. Then, the pros and cons of the two solar collectors are also discussed and compared. The advanced exergy analysis is a powerful tool to show the potential of room for improvement [43] and it is rarely used for solar collectors. In this study, it is adopted to evaluate avoidable and unavoidable exergy destruction and provide reasonable development direction to the designers.

The layout of this paper is arranged as follows. The experimental test platform and traits of two structurally optimized solar collectors are described in Section 2. The numerical model and evaluation methods are stated in Section 3. For the brief purpose, some detailed equations are placed in the Appendix. The experimental and numerical results of their energy and exergy performance are exhibited in Section 4 and Section 5, respectively. In Section 6, a discussion for two solar collectors is conducted about their unique structure and improvement potential.

2. Experimental platform description

An experimental platform is constructed that includes the structurally optimized ETSC and EFPC (see Fig. 2). These two solar collectors are self-innovate developed and cooperatively manufactured by Beijing Jinyang Solar Co., Ltd and TVP Solar [44]. They are both mounted south-oriented and with a 30° slope. The test period is selected between 11:00 and 13:00 during the daytime with maximal solar irradiance.

The detailed internal structures and general energy flow direction of two solar collectors are exhibited in Fig. 3. The EFPC is featured as the plate structure, such an issue will cause the glass cover to suffer great stress from the atmosphere. To solve this problem, a pillar array is needed to avert fracture. Since the solar collector is designed for intermediate temperature conditions, thermal stress induced by uneven temperature distribution is unavoidable during the work process. To mitigate the large thermal expansion and contraction, the absorber plate is divided into two parts on the central axis. Corresponding to this design, as the heat transfer fluid (HTF) flow route shown in Fig. 3 (a), the HTF flow is also separated and the downside pipes will be connected to the upper ones to form a complete fluid circulation.

The ETSC employs heat pipes for heat exchange, so the HTF will not enter evacuated tubes. This technology enables more efficient heat transfer and more stable operation. Besides, a more uniform stress distribution is realized with the contribution of the tubular shape of ETSC.

Water is used as HTF for two kinds of non-concentrating solar collectors. It is supplied by a mold temperature controller, which can adjust the inlet temperature in a certain range (<1 °C). When the outlet HTF from the mold temperature controller is higher than the setting value, it will make the hot HTF mixed with the cold one. When the outlet temperature is lower than the setting value, the electrical heater will heat the HTF to the anticipated value. The mold temperature controller is configured with a pressurization system to prevent the water from vaporization when the temperature goes up. A circulation pump is also integrated to maintain the HTF cycling in the solar panel.

Pt-100 resistance temperature detector is used at the inlet and outlet of the solar collector. An electromagnetic flowmeter is added to the inlet pipe of the solar collector. All the measurement apparatus is connected to a data acquisition instrument and the data is recorded each 10s. During the actual process, the same test condition is repeated four times with each lasting at least 3 min for the precision purpose. Since the outdoor test is vulnerable to weather conditions and the whole system has time-dependent fluctuations, each test point has 12 min reservation [45] before data acquisition (see Table 1).

To prove the accuracy of the experiment results, the uncertainty of the experiment is calculated by the error propagation formula [46].

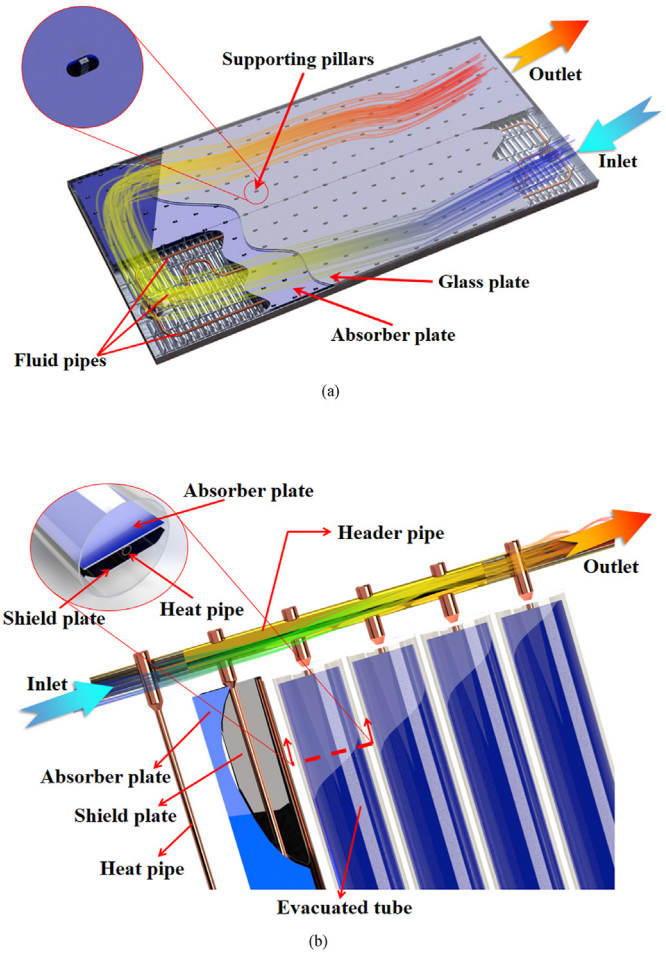

Fig. 3. The diagrammatic structure of (a) EFPC and (b) ETSC.

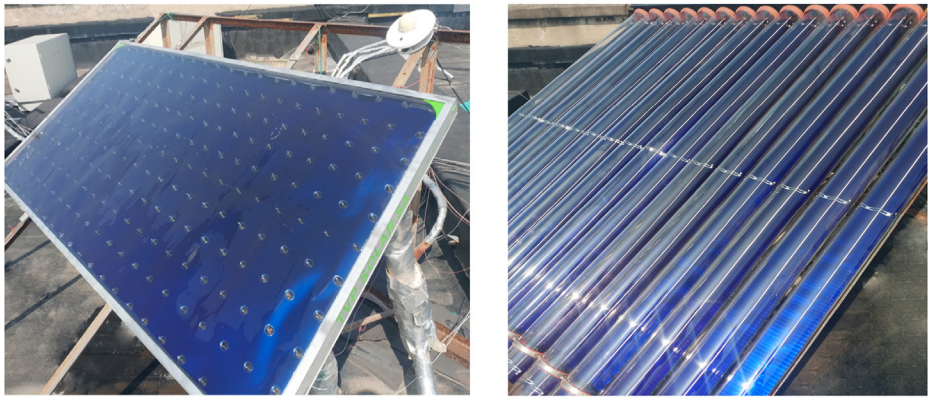

Fig. 2. Test rig of (a) EFPC and (b) ETSC.

Table 1
The parameters of work apparatus and their precision.

Working apparatus	Measurement range/precision
Mold temperature controller	10–180 °C (1 °C)
Solar pyranometer	0-2000 W/m^2 (0.1 W/m^2)
Anemograph	0.1 m/s
Pt-100	0.1 °C
Flow meter	0.5%

$$RE_\eta = \sqrt{\sum_{i=1}^{n}\left(\frac{\Delta x_i}{\eta}\right)^2} \tag{1}$$

where η is the efficiency and x is the direct measurement result (such as the mass flow rate, temperature, and so on.). According to the error value in Eq. (1), the uncertainty of the experiment is 2.2% that can be regarded as sufficient for this study.

3. Methodology

3.1. The energy and exergy analysis for the experiment data

The experiment is carried out in the natural environment so the boundary conditions (such as solar irradiance, ambient temperature, etc.) are varying at every moment. The normalized temperature difference T_i* [47] is used to describe the thermal performance which involved the inlet temperature, ambient temperature, and solar irradiance at the same time, so it can reflect the thermal efficiency of the solar collector comprehensively. For a more accurate result of solar collector, the normalized temperature difference T_i* and thermal efficiency η is tested under steady-state conditions, i.e. select the experiment results that the boundary condition parameters fluctuate in a narrow range at the time of testing.

$$T_i^* = \frac{\overline{T_i} - \overline{T_{amb}}}{\overline{G}} \tag{2}$$

where T_i is the inlet temperature (K), T_{amb} is the ambient temperature (K), and G is the solar irradiance (W/m^2). The top bar means this variable is the average value for the steady-state experiment period.

The thermal efficiency of the whole solar field is calculated as [48]:

$$\eta = \frac{\overline{\dot{m}} c_{p,w}(\overline{T_o} - \overline{T_i})}{A_{SF}\overline{G}} \tag{3}$$

where the $\dot{m}$ is the mass flow rate (kg/s), $c_{p,w}$ is the specific heat capacity (J/(kg·K)), T_o is the outlet temperature (K), and A_{SF} is the solar collector's area (m^2).

From the 2nd law of thermodynamic, we have established the exergy model for the exergy analysis of the two structurally optimized solar collectors. The solar irradiance is absorbed by the solar collector and converted to the enthalpy exergy of the HTF. The increase of enthalpy exergy in the heat pipe is calculated from Eq. (4) [49].

$$E_{gain} = \dot{m}[h_2 - h_1 - T_{amb}(s_2 - s_1)] \tag{4}$$

where the h_2, h_1 refer to the specific enthalpy of the HTF at the outlet and inlet of the solar collector (J/kg), and s_2, s_1 is the specific entropy of the HTF at the outlet and inlet of the solar collector (J/(kg·K)).

The solar irradiance exergy from the sun is [50]:

$$E_s = GA_{SF}\psi \tag{5}$$

$$\psi = 1 - \frac{4}{3}\frac{T_{amb}}{T_s} + \frac{1}{3}\left(\frac{T_{amb}}{T_s}\right)^4 \tag{6}$$

where ψ is the maximum available energy ratio from the solar irradiance and it can be calculated from Petela [51]. T_s is the black body temperature of the sun and is generally assumed as 6000 K [52].

The exergy of the solar collector is defined as [49]:

$$\eta_{ex} = \frac{E_{gain}}{E_s} = \frac{\dot{m}(h_2 - h_1 - T_{amb}(s_2 - s_1))}{GA_{SF}\psi} \tag{8}$$

Eq. (8) can be also be written in from of the exergy loss [49]:

$$\eta_{ex} = 1 - \frac{E_{loss}}{GA_{SF}\psi} \tag{9}$$

3.2. Numerical model evaluation

The numerical model about ETSC and EFPC is established according to their actual structure and thermodynamic law. The detailed model is presented in Appendix A and B. The relative error between the experiment and simulation result can be accessed by root mean square error which is defined as [53]:

$$RMSD = \sqrt{\frac{\sum_{1}^{n}\left[(X_{sim,i} - X_{exp,i})/X_{exp,i}\right]^2}{n}} \times 100\% \tag{10}$$

where, $X_{sim,i}$ and $X_{exp,i}$ are the results of i_{th} simulation and experiment, respectively.

4. Experiment results and model validation

4.1. Energy performance

Based on the steady-state experiment, the normalized temperature difference fitted curve of two non-concentration solar collectors can be obtained. Considering the ETSC has a gap between each glass tube, its thermal efficiency calculation has accounted for these gap regions when calculating the total solar irradiance. Likewise, the trepanning area of EFPC is also involved in the evaluation. As displayed in Fig. 4, in the whole axis, i.e. the low and intermediate temperature range, the thermal efficiency of EFPC is higher than ETSC. Under the same absorber area, the ETSC has a larger glass cover area which leads to a larger outside heat transfer area. Besides, the structure of EFPC makes both the inlet and outlet copper tubes sealed under vacuum, thus the heat loss of the header tube of ETSC is evaded.

According to the experimental data, the intercept efficiency of EFPC is 17% higher than ETSC, and the thermal efficiency is 64.4% and 54.2% for both solar collectors at the operating temperature of 100 °C. Their thermal efficiencies get closer in the high normalized temperature difference value (i.e. high inlet temperature) because the EFPC has a higher outlet temperature which leads to a higher radiation heat loss.

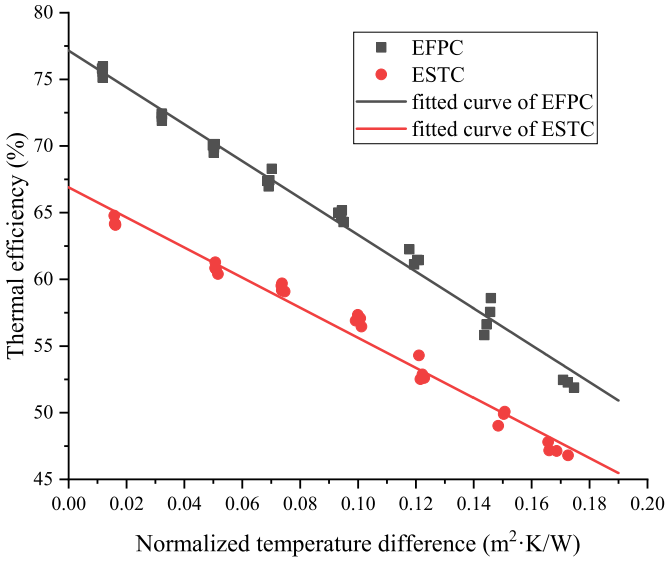

Fig. 4. The fitted curve of the normalized temperature difference of these two solar collectors.

4.2. Exergy performance

An exergy efficiency comparison of ETSC and EFPC is conducted in Fig. 5. The tested temperature range varies between 60 °C and 200 °C. It is noticed that the exergy efficiency of EFPC is still higher than ETSC in the intermediate temperature range. The reason there exists the best exergy efficiency in Fig. 5 is the competition of the following two processes. On one hand, the outlet exergy increase with the operating temperature; on the other hand, the temperature difference between inlet and outlet temperature becomes much smaller when the operating temperature goes up and the enthalpy and entropy difference is narrowed. The EFPC has attained its maximum exergy efficiency of 17.0% at 151 °C and ETSC's maximum exergy efficiency is 15.3% at 156 °C.

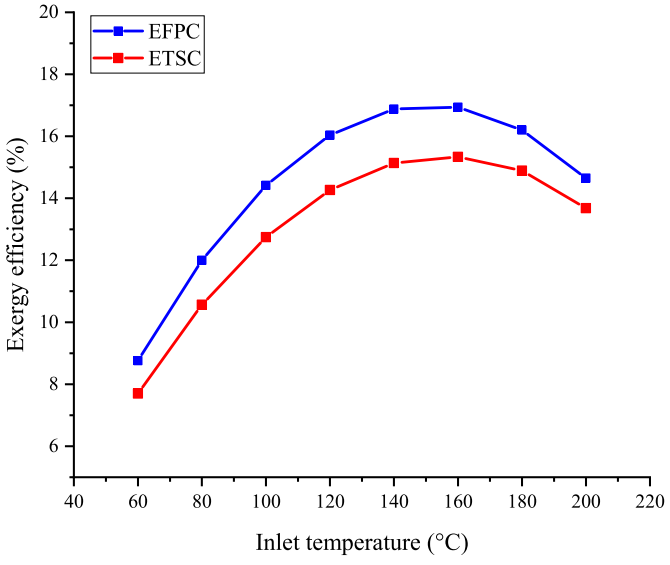

Fig. 5. Exergy efficiency results of the ETSC and EFPC under different inlet temperatures.

4.3. Model validation

The established numerical model for the EFPC in Appendix B is validated by the experimental results. The thermal and exergy efficiencies of the EFPC are displayed in Fig. 6, the relative error between the numerical and experimental results is 1.6% and 1.8%, respectively. The numerical model for the ETSC has been validated in Ref. [54] and also obtained acceptable results of 1.5%. Therefore, this numerical model is qualified for the prediction of both solar collectors' performance and it's considered reasonably accurate for use in further analysis.

5. Numerical analysis of two solar collectors

5.1. Thermal resistance networks

Essentially, the structural optimization of two solar collectors is the changing of their internal thermal resistance network. The thermal resistance diagrams of the structurally optimized ETSC and EFPC are illustrated in Fig. 7. In light of the structure of ETSC, the shield plate is added as an additional series thermal resistance for hindering the radiant heat loss. Also, the vacuum for the flat plate solar collector is equivalent to reducing the parallel thermal resistance. Hence, both of them can minimize the thermal loss of the original structures.

For quantitative analysis, a typical working condition is chosen, where the solar irradiance is 800 W/m^2, the flow rate is 0.03 kg/s, the ambient temperature is 25 °C, the inlet temperature is 80 °C, and the wind velocity is 2 m/s . With the validation model of two solar collectors, each thermal resistance in Fig. 7 is calculated and the results are shown in Table 2 and Table 3. It is noticed that the additional heat shield plate of ETSC has improved the thermal resistance between the absorber plate and glass tube significantly. The original structure absorber has heat radiative transfer to the whole glass tube, which will cause great heat loss from the absorber plate to the ambient and ground. The shield plate has made compensation for this parasitic shortcoming. The thermal resistance has been elevated 3.83-fold over the original structure.

The EFPC uses a glass plate substitute for the glass tube and a backplate that has less specific surface area than the glass tube. In comparison with the original structure, i.e. flat plate solar collector, reducing the parallel thermal resistance also plays a vital role in the solar capture process. The thermal resistances between the bottom side of the absorber plate and glass plate have been upgraded 4.17-fold. Therefore, the great heat loss of these two non-concentrating solar collectors has been mitigated substantially.

5.2. Energy flow investigation

To elucidate the energy conversion and loss during the solar harvesting process, the energy flow from solar energy to useful energy of the two solar collectors is presented in Fig. 8. The total input energy is set with the same solar irradiance and the energy flow direction is depicted clearly. The inherent solar energy loss occurs on two solar collectors: the EFPC has a trepanning on the absorber plate to provide space for the supporting pillars and ETSC has a gap between each glass tube.

As shown in Fig. 8, the most energy loss for both solar collectors occurs on the glass plate or tube owing to the optical loss and emitted radiative loss. Based on this phenomenon, the shield plate is instrumental for reducing radiative loss from the absorber plate. It is observed that the shield has a crucial effect for restraining the heat radiation from the bottom of the absorber plate. Only 1.68% energy loss occurs on the bottom side of the absorber plate on ETSC while the EFPC has 6.33% energy loss at the same position.

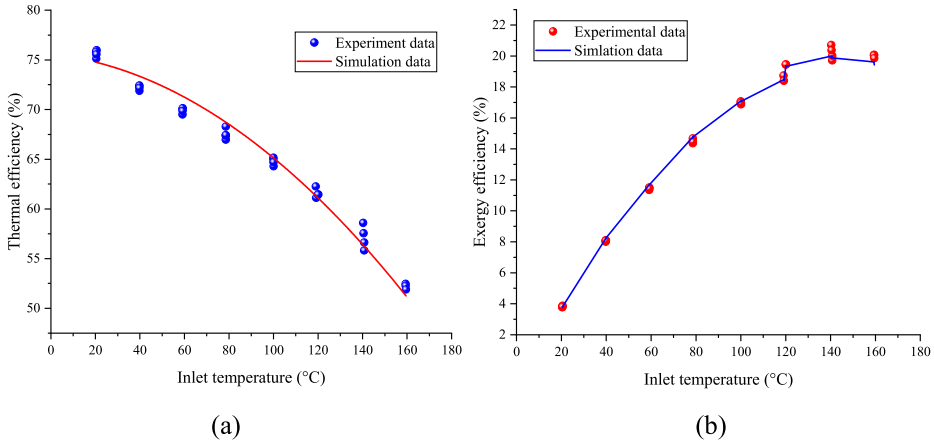

Fig. 6. The numerical model verification of EFPC (a) thermal efficiency (b) exergy efficiency.

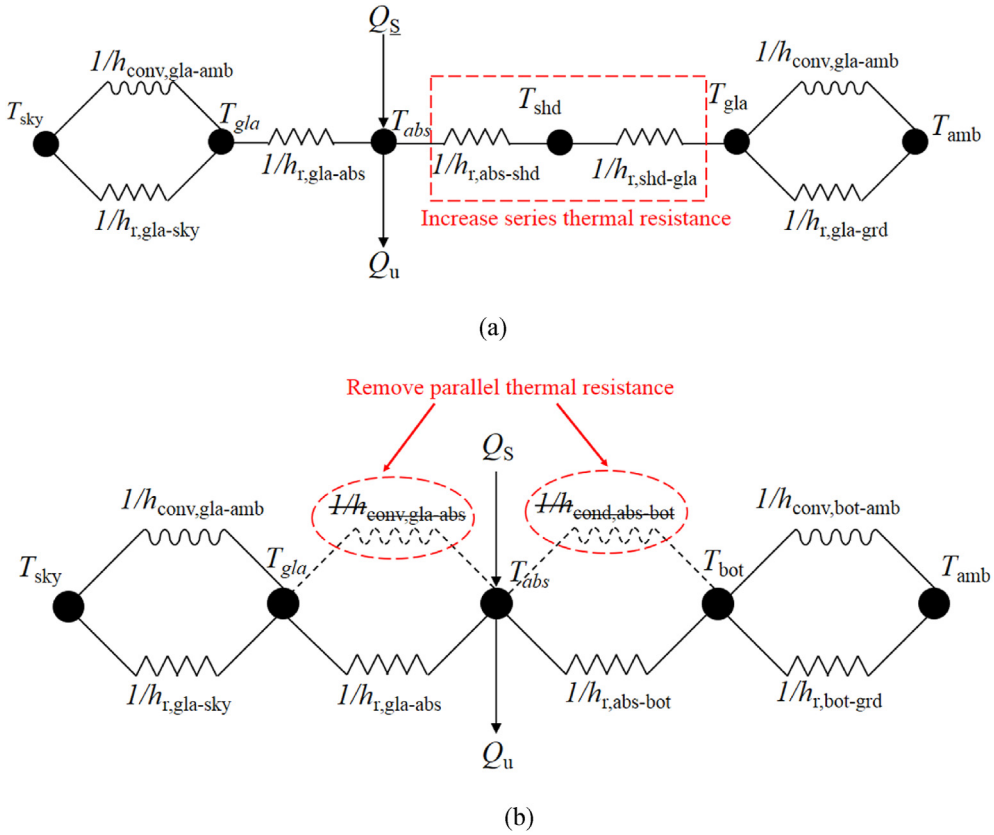

Fig. 7. The thermal resistance of (a) the structure optimized ETSC and (b) structure optimized EFPC.

Table 2
Thermal resistance distribution of the ETSC.

ETSC	$R_{gla-sky}$	$R_{gla-abs}$	$R_{abs-shd}$	$R_{shd-gla}$
Original structure	0.0191	1.4937	1.3713	
Optimized structure	0.0095	1.4763	2.5916	2.6667

Table 3
Thermal resistance distribution of EFPC.

EFPC	$R_{gla-amb}$	$R_{gla-abs}$	$R_{abs-bot}$	$R_{bot-amb}$
Original structure	0.0958	0.2944	0.6659	0.1000
Optimized structure	0.0028	1.4526	2.5609	0.1001

However, for reducing the upper side radiative loss of the absorber, the high transmissivity material (i.e. infrared thermal mirror [55,56]) is required for the heat radiation recovery that is not easy to be achieved. The results from Ref. [57] discussed the required property for this material to further decrease the radiative heat loss of EFPC that is worth researching in the future.

It is also noticed that the proportion of trepanning energy loss on the EFPC is only 3.27%. However, the gap loss of ETSC accounts for a considerable energy loss (9.85%) during the solar energy capture process, thereby impairing the thermal performance more

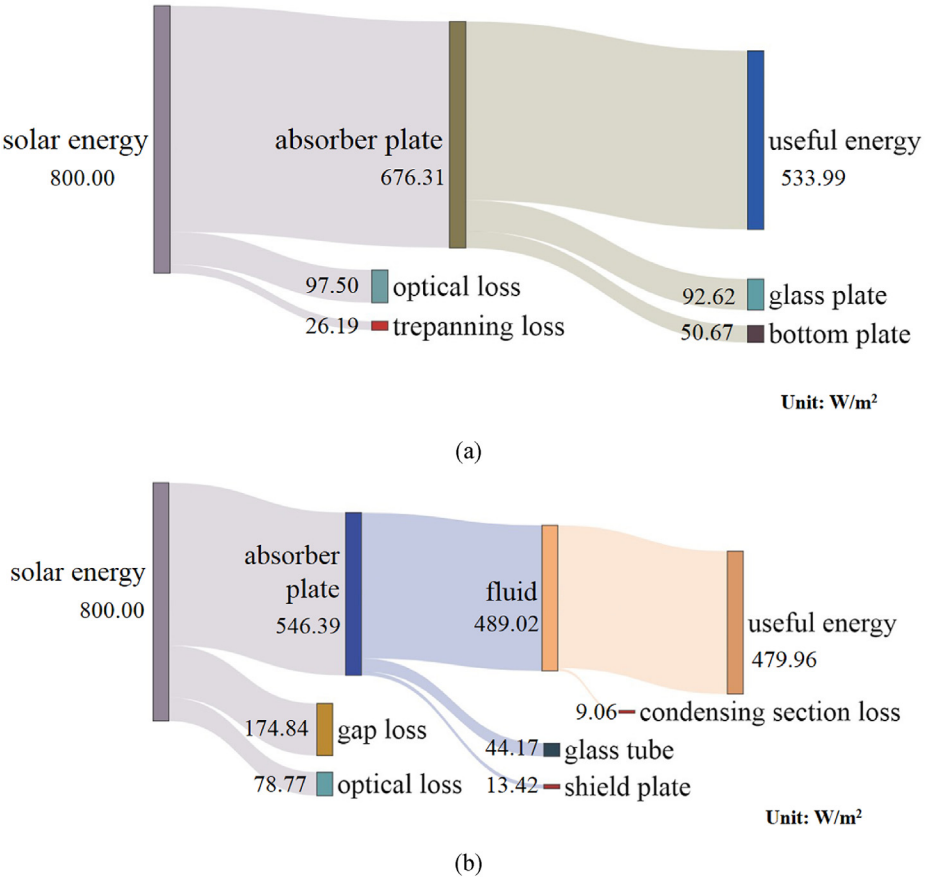

Fig. 8. The energy flow chart of (a) EFPC and (b) ETSC.

seriously. Although the ETSC has added a series thermal resistance to prevent heat radiation losses, it obtains less useful energy than EFPC since the heat losses on the tubes' gap and condensing section are not ignorable.

5.3. Exergy destruction breakdown

In this section, a numerical analysis of the exergy loss breakdown for these two kinds of solar collectors is carried out. The solar irradiance is set at 800 W/m^2, the ambient temperature is set at 25 °C, and the HTF flow rate is set at 0.06 kg/s as the working conditions.

First, the exergy flow charts of two solar collectors are obtained under the circumstance that the operating temperature is 150 °C. It is noticed that the vastest exergy destruction of both solar collectors is the solar-thermal conversion process on the absorber plate, i.e. the solar energy is converted to thermal energy. This can be ascribed to the absorptivity coefficient of the absorber plate and the great temperature divergence between the sun and absorber plate. On the one hand, the higher absorptivity coefficient of the absorber plate can capture more solar energy such that the exergy loss will decrease. On the other hand, the sun is usually considered as a black body with 6000 K, so the enormous temperature difference will bring about massive exergy loss. This exergy loss part is related to the analysis method for the solar exergy. According to the updated literature [58], the solar exergy is reappraised comprehensively with the geometric factor, absorber property, etc. involved. This new method will decrease this exergy loss for practical solar systems. The same portion of exergy loss in EFPC is a little higher than ETSC since the surface area of the absorber plate on EFPC is larger than ETSC.

In Fig. 9 (a), the gap loss refers to the solar irradiance passing through the gap between two glass tubes, while the interval loss denotes the solar irradiance that passes through the interval between the glass tube and absorber plate since they cannot contact. These two parts are inevitable and they account for a considerable amount of loss compared to the trepanning loss in Fig. 9 (b). In the heat transfer process that takes place on the absorber plate, the exergy is destructed more gravely on the EFPC due to the larger plate area. Since the heat pipe is employed in ETSC, one more heat transfer procedure is involved in it. Fortunately, the heat pipe does not have a noticeable impact on the exergy flow. Rather, it is the heat transfer process that happens on the condensation section that causes large exergy destruction from the condensation section to the HTF as it dissipates to the surroundings. On the EFPC, the heat absorber tubes are surrounded by a vacuum environment, so the exergy dissipation to the ambient surroundings only occurs on the bottom and glass plate.

Each exergy destruction part in Fig. 9 will vary with respect to the operating temperature as displayed in Fig. 10. The solar-thermal conversion exergy destruction part will decrease with the increase of the absorber plate's temperature. In Fig. 10 (a), the exergy loss triggered by solar irradiance missed from the ETSC's gap and solar-thermal conversion on glass tube is immobile of the entire low and intermediate temperature range. This phenomenon is attributed to the fixed transmittance of the glass tube and its almost constant temperature level. On account of the temperature difference between the copper tube and HTF narrows, the exergy loss caused by

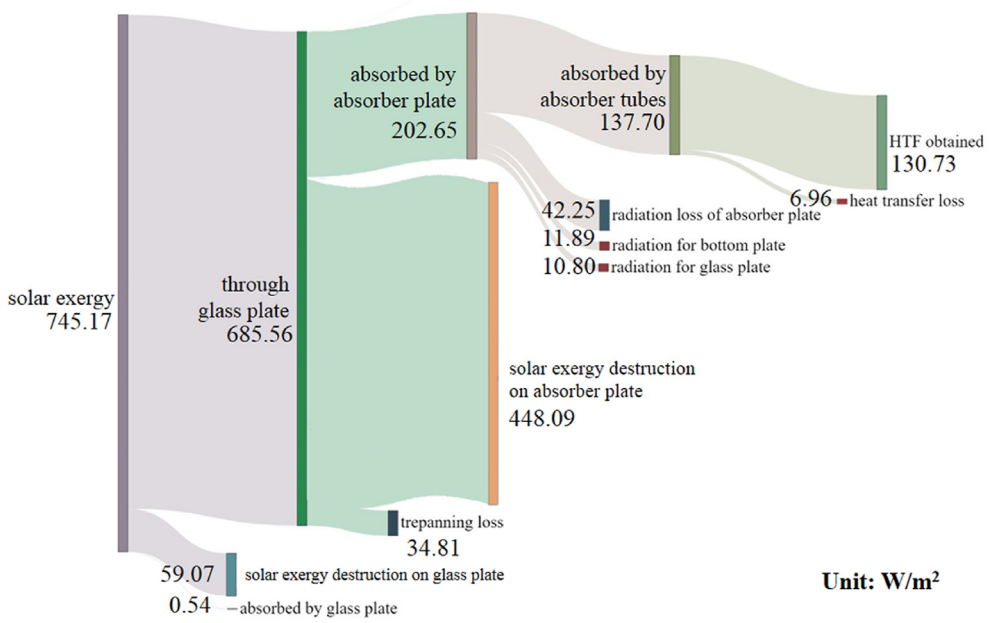

(a)

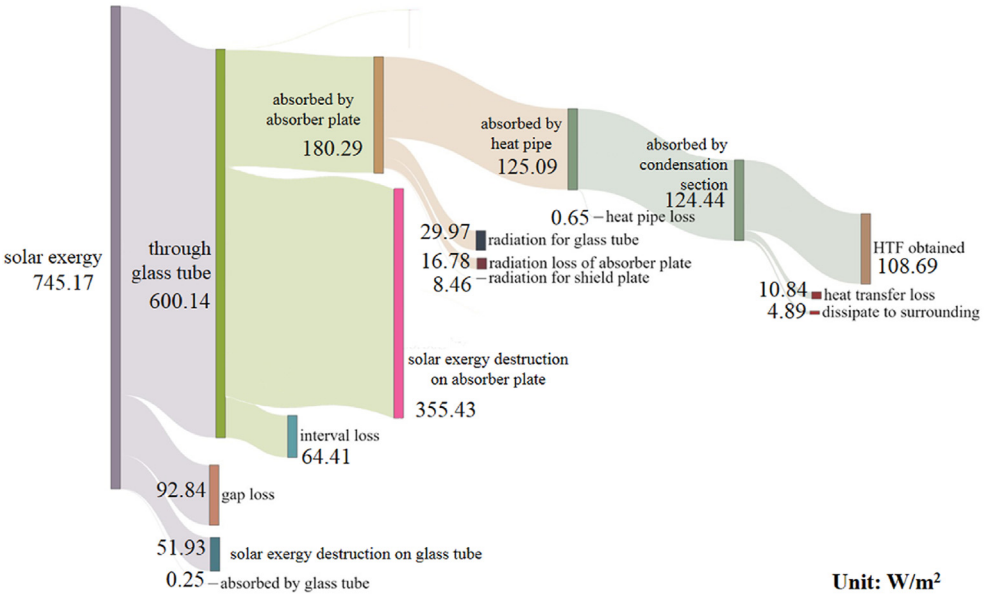

(b)

Fig. 9. Exergy flow charts of the (a) EFPC and (b) ETSC.

heat transfer from the copper tube is decreasing with the inlet temperature.

It is noticed that the radiation exergy loss from the absorber plate to the glass tube and shield plate is escalating with the inlet temperature. It is caused by the temperature difference between the absorber plate and the other two bodies. Besides, the radiation exergy loss between the absorber plate and the glass tube is higher than the shield plate which demonstrates that the shield plate can suppress the radiation loss efficiently.

It can be observed that the heat transfer loss in EFPC is smaller than ETSC. The reason for that is the average HTF temperature of EFPC is higher than ETSC which leads to a smaller exergy loss. Another more important reason is the exergy loss in the condensation section of ETSC is non-ignorable. The radiation from the absorber plate to the bottom plate and glass plate is almost close to each other due to their temperature values being almost identical.

6. Discussion

Based on the previous experimental and numerical results, some pros and cons of EFPC and ETSC have been revealed. The gaps on the ETSC will cause extra energy and exergy losses while the shield plate works oppositely. The condensation section is also important in the heat transfer process of ETSC. The trepanning on EFPC will cause the declination of energy and exergy but plays a key

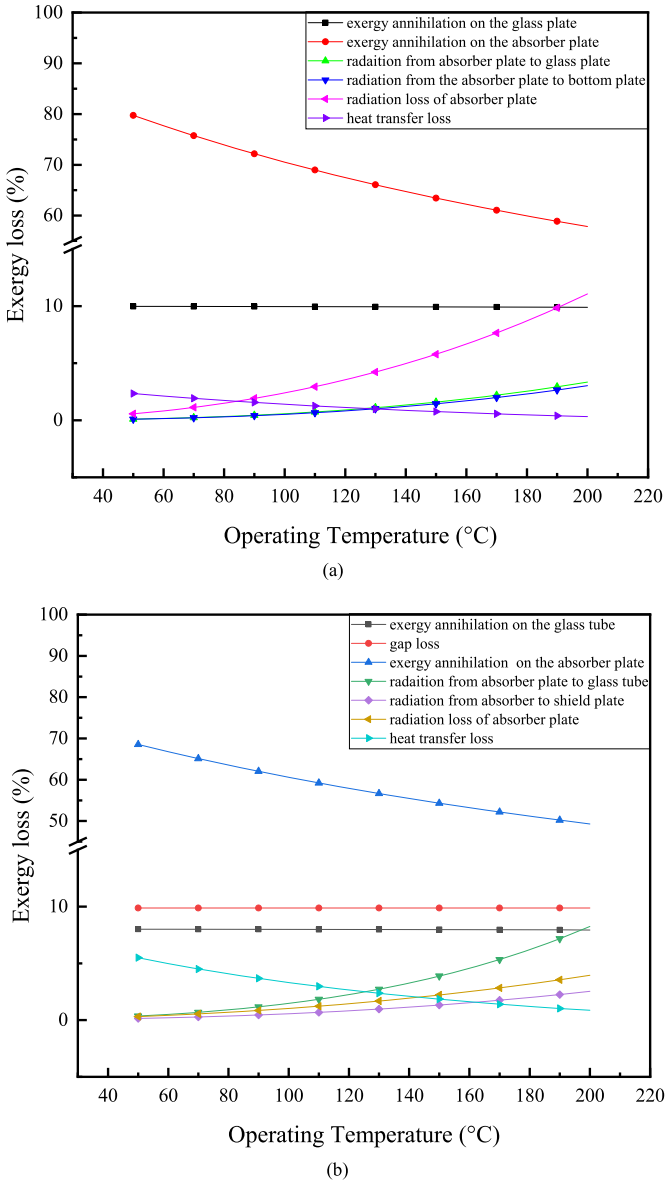

Fig. 10. Exergy loss breakdown under different operating temperatures of the (a) EFPC and (b) ETSC.

role in withstanding the atmospheric pressure. Hence, in this section, an exhaustive discussion about these components and their thermodynamic properties is conducted. Moreover, the improvement space for these two solar collectors is investigated via advanced exergy analysis methods.

6.1. The effect of shield plate for the structure optimized ETSC

As previous results have shown, the shield plate plays a vital role in the energy and exergy performance of ETSC. Hence, the thermal property of the additional shield plate is a consequential design parameter for ETSC. The emissivity of the shield plate will have a great influence on the radiant heat dissipation process. With the low inlet temperature, the thermal efficiency of ETSC remains steady (it declines by 2.67% when the inlet temperature is 50 °C). With a higher inlet temperature, the thermal efficiency decreases a lot, and the effect of the shield plate's emissivity is also magnified. The thermal efficiency declines by 28.38% when the inlet temperature is 200 °C (see Fig. 11).

6.2. The length distribution on the heat pipe

Another pivotal component of the ETSC is the heat pipe, which consists of the evaporation section and the condensation section. The solar absorption and heat discharge processes are dominated by these two parts, thereby concerning the thermal performance of the solar collector. Hence, the length ratio of the evaporation and condensation section is worth researching to achieve better thermal performance. As illustrated in Fig. 12 (a), the maximum evaporation section length ratio occurs at 0.74 of the thermal efficiency occasion. Fig. 12 (b) manifests that the maximum evaporation length ratio occurs at 0.81 of the exergy efficiency occasion.

It is noticed that the thermal and exergy efficiency fall sharply after the evaporation section ratio is beyond 0.9. The overlength evaporation section results indicate that the heat may accumulate in the condensation section and lack enough area to release heat for the HTF. Therefore, the proportion of the two sections should be no more than this threshold value so as not to affect the thermal performance significantly. The above outcome indicates that the current design (the proportion of evaporation section is 0.96) hinders the heat transfer performance in the condensation section. Given more aperture area is expected and manufacturing technique requirement in the real applications, the evaporation section length is usually immutable. Accordingly, as an important tache of the heat transfer process in ETSC, some heat transfer enhancement methods can be implemented in such an important position.

6.3. Surface mechanical stress analysis

One of the main obstacles of EFPC fabrication is the surface mechanical stress problem. The huge atmospheric pressure will cause too much deformation of the glass cover to crack. This problem is avoided on the ETSC because of its innate advantage of tube shape. As shown in Fig. 13, the deformation of an evacuated glass tube is depicted under standard atmospheric pressure. Assuming the upper end of the tube is restrained by supporting structure, the finite element method analysis reveals that the maximum displacement of the entire tube is 0.035 mm which is small enough for operating safety. Moreover, according to the

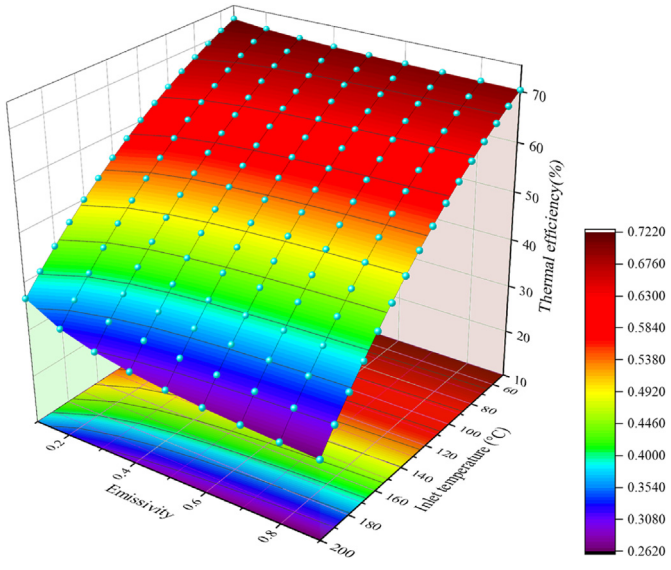

Fig. 11. Thermal efficiency at different emissivities of the shield plate.

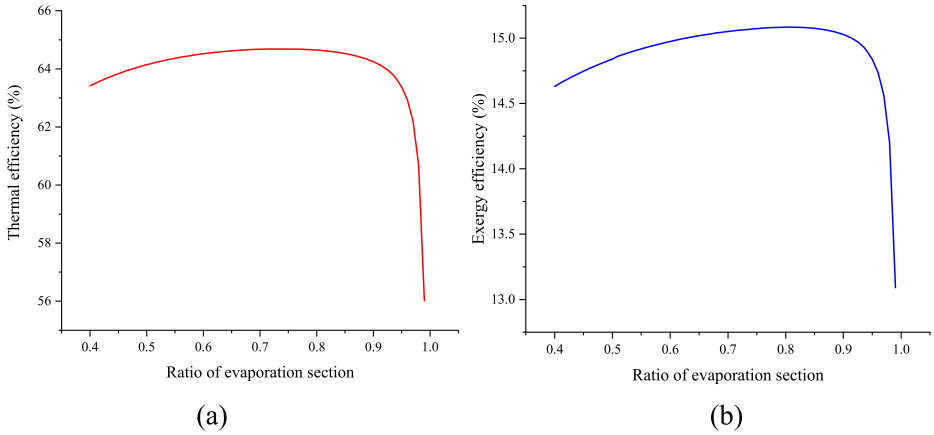

Fig. 12. The influence of the length ratio of evaporation section, (a) thermal efficiency and (b) exergy efficiency.

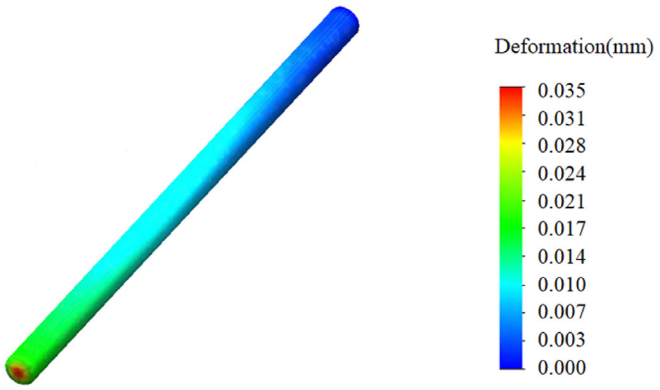

Fig. 13. The finite element analysis of ETSC's tube.

previous section, the temperature of the glass tube is not much higher than the ambient temperature so the thermal-induced stress can be omitted.

The EFPC processes a giant glass plate cover that is similar to the cantilever beam structure if there is only a housing support structure around it. In the practical application, the aperture area of the solar collector is usually around 2 m^2. In Fig. 14 (a), a finite element analysis is conducted for the case when the glass plate cover is only supported by the edge structure. The result indicates that the maximum deformation is as high as 23.54 mm. Hence, the glass cover will crack during the vacuuming process in the real manufacturing process. However, if a pillar array is added under the glass plate cover, the situation will be significantly improved. It is noticed that the maximum deformation is alleviated to only 0.041 mm with pillars' support. Even though it will cause a little curtailment of the absorber plate's area, the major challenge for materializing EFPC is addressed.

As depicted in Fig. 15, the maximum deformation of the glass plate is varying under different pillar arrangements. The fewer pillars lead to less trepanning area and more solar energy will be captured. The trepanning loss in Fig. 8 (a) will have less influence on the resulting thermal efficiency. The maximum deformation increases sharply when the pillars are less than 16 × 8, which will cause the glass plate vulnerable to crack under the atmospheric pressure.

6.4. Advanced exergy analysis

The conventional exergy analysis method can only point out the amount of exergy destruction on each heat transfer process, while the advanced exergy analysis can determine how much the exergy destruction can be avoided, i.e. reduce the irreversibility. With the development of technology on solar collectors, some components could be enhanced to avoid the exergy destruction that is called "avoidable exergy destruction". However, there will always be a part of exergy destruction that cannot be avoided owing to the structure, physical, or economic restraints. These parts are called "unavoidable exergy destruction". In this section, the working situation of two solar collectors will be assumed in a hypothetical condition (see Table 4 and Table 5), so that the avoided and unavoidable exergy destruction can be determined. The concrete theory and calculation method are laid in Appendix D. The hypothetical condition can be realized with the progress of technology in the future and it is referenced from the results of cutting-edge researches for reasonable values. Thus, this analysis is instructive for the further development of non-concentrating solar collectors.

As shown in Fig. 16, the internal sector diagram is the original exergy destruction (based on the results from Section 5.3) while the outer sector diagram is the avoidable and unavoidable exergy destruction for each part. It is observed that the shrink of gaps on the ETSC leads to 51.27% (74.35 W/m^2) exergy destruction on glass tubes avoidable as shown in Fig. 16 (b). While 39.47% (23.53 W/m^2) exergy destruction of the glass plate on EFPC will be avoidable with only the changes of optical property. 5.77% (24.24 W/m^2) exergy destruction on the absorber plate can be avoided on the ETSC. Owing to the aforementioned reasons, this exergy destruction is more the results of exogenous. However, by reducing the trepanning numbers and improving the absorber plate simultaneously, 10.74% (51.85 W/m^2) exergy destruction could be avoided on the EFPC. As discussed before, the trepanning arrangement reduction only has a little influence on the glass deformation.

It also can be seen that 27.95% (4.39 W/m^2) and 14.37% (1.00 W/m^2) exergy destruction can be avoided in the condensation section of ETSC and absorber tubes of EFPC, respectively. From the perspective of quantity, although it accounts for a small proportion of the total exergy destruction, this part is situated separately at the last heat transfer process in two solar collectors according to Fig. 9. In other words, this part has a higher "exergy grade" to influence the final exergy output in the HTF. For the ETSC, the avoidable exergy can be realized by heat transfer enhancement methods acting on the condensation section, corresponding to the previously presented discussion. For the EFPC, some measures also can

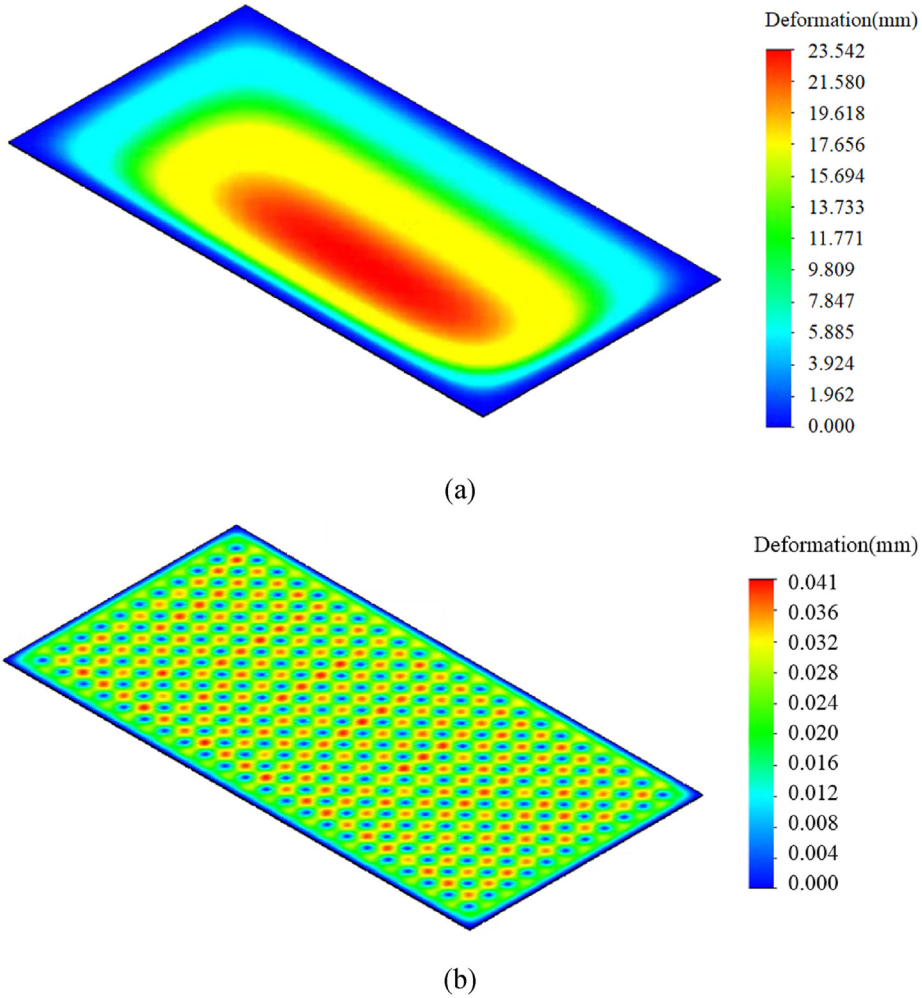

Fig. 14. The finite element analysis of EFPC, (a) only edge restrain and (b) with support pillars.

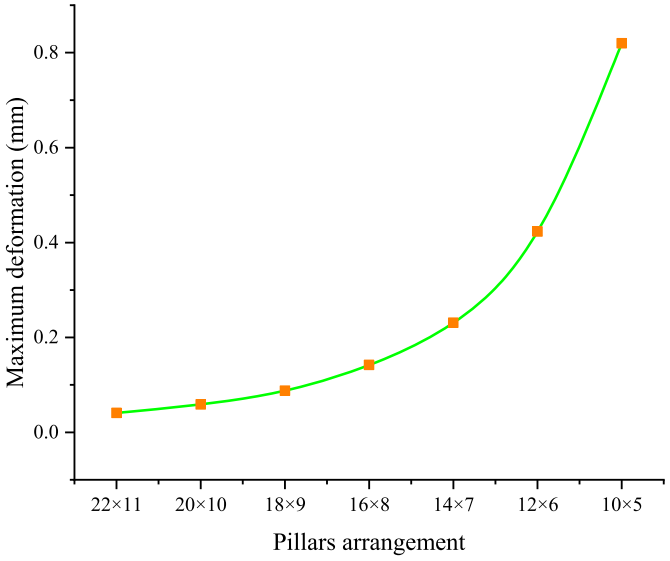

Fig. 15. The maximum deformation of glass plate under different pillar arrangements.

be implemented on the absorber tubes, such as the nano-fluid to increase the heat transfer coefficient [48].

Table 4
The hypothetical working condition of ETSC.

Parameters	Real condition	Hypothetical condition	Ref.
τ_{gla}	0.92	0.95	[59]
ε_{gla}	0.88	0.20	[60]
α_{gla}	0.05	0.02	[60]
A_{gap}	0.46 m^2	0.20 m^2	\
α_{abs}	0.95	0.97	[61]
$\varepsilon_{abs,top}$	0.1	0.05	[60]
$\varepsilon_{abs,bot}$	0.08	0.05	[60]
A_{con}	0.0044 m^2	0.01 m^2	Results from Section 6.2
k_{ins}	0.06 W/(m·κ)	0.02 W/(m·κ)	[62]

It is worth noting that if the hypothetical situation is realized, the total exergy destruction can be reduced by 17.74% (102.99 W/m^2) and 13.90% (76.39 W/m^2) in the ETSC and EFPC, respectively. Therefore, this advanced exergy analysis provides a more reasonable and realistic measure to the designers and the most attention should be paid to the glass cover and structure close to the HTF.

7. Conclusions

To exploit the internal energy and exergy transfer and stress relationships among the components, the essential influence of structural optimization on performance improvement, and exploit

Table 5
The hypothetical working condition of EFPC.

Parameters	Real condition	Hypothetical condition	Ref.
τ_{gla}	0.92	0.95	[59]
ε_{gla}	0.88	0.20	[60]
α_{gla}	0.05	0.02	[60]
α_{abs}	0.92	0.97	[61]
$\varepsilon_{abs,top}$	0.035	0.05	[60]
$\varepsilon_{abs,bot}$	0.08	0.05	[60]
N_{tre}	22 × 11	16 × 8	Results from Section 6.3
h_c	According to HTF's property	50% enhanced	[63,64]

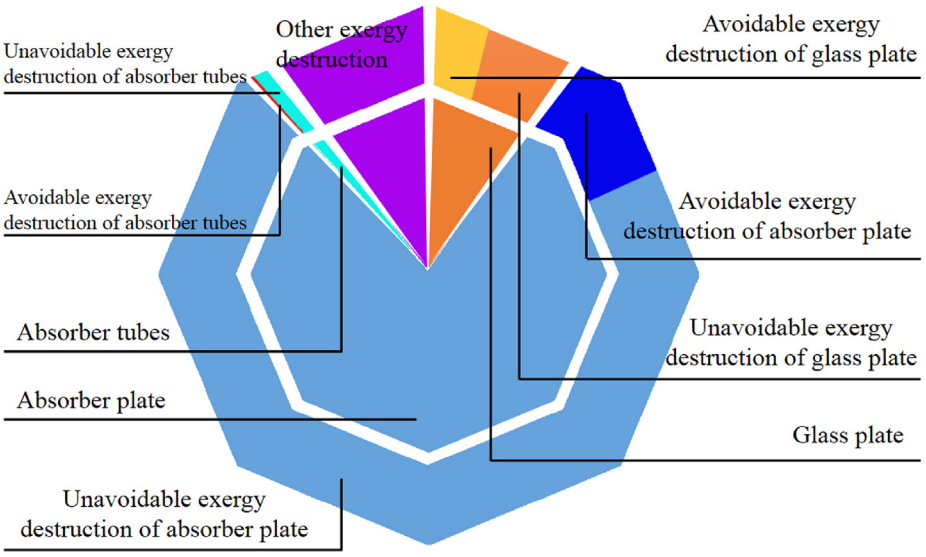

(a)

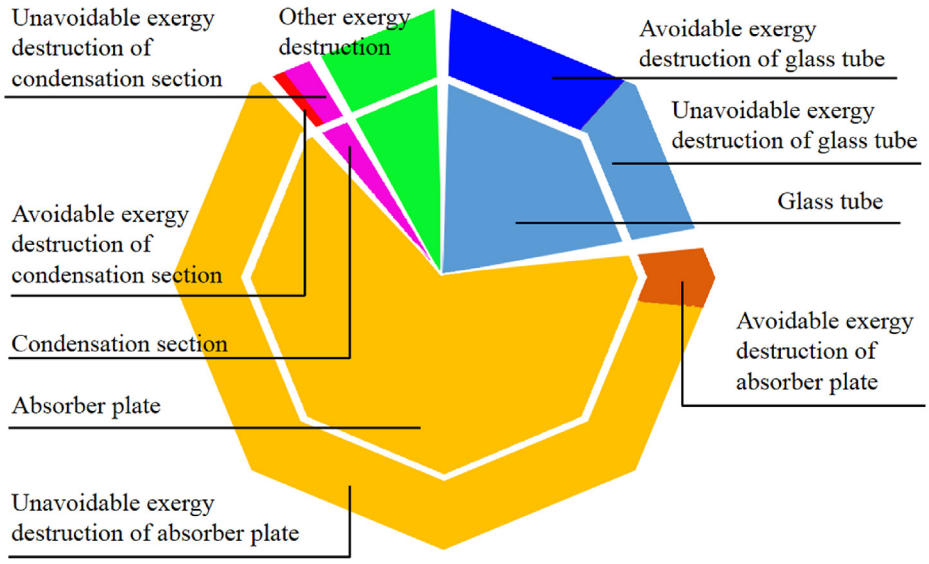

(b)

Fig. 16. The avoidable and unavoidable exergy destruction of (a) EFPC and (b) ETSC.

further development potential of the non-concentrating vacuum-type solar collectors for the intermediate temperature applications, a detailed comparison of two structurally optimized solar collectors is executed in this paper. The experimental research and theoretical analysis of these two kinds of collectors are carried out respectively. The main conclusions are drawn as follows.

1. The structural improvement can alter thermal resistance on the two solar collectors. The addition of series thermal resistance or removal of parallel thermal resistance will render 3.83 and 4.17-fold thermal resistance enhancement in the corresponding heat transfer process, respectively. Therefore, the structural improvement has a great contribution to altering the thermal resistance, thereby improving the thermal performance of the non-concentrating solar collectors.
2. The land source is valuable for solar energy applications, especially in densely populated regions. The gaps between the evacuated tube solar collectors cause massive solar irradiance losses, and more floor area space is needed accordingly. The advanced exergy analysis manifests that it will cause 51.27% of avoidable exergy destruction. Whereas the trepanning loss of evacuated flat plate solar collector leads to 10.74% avoidable exergy destruction, which has much less effect on the thermal efficiency.
3. The ratio of condensation and evaporation length has a considerable influence on the heat transport process of the heat pipe. The heat transfer enhancement method can be added to the condensation section of the heat pipe evacuated tube collector.
4. The support pillar is critical of the stress distribution of evacuated flat plate solar collectors and it can greatly reduce the deformation of the glass plate. A more reasonable pillar arrangement can be implemented for better performance while maintaining safe operation.
5. Based on the hypothetical working condition for both solar collectors, the advanced exergy analysis demonstrates that the total exergy destruction can be reduced by 17.74% and 13.90% in heat pipe evacuated tube collector and evacuated plate flat solar collector, respectively.

The results of this paper are instrumental for the further development of non-concentrating solar collectors. For future studies, the effort will be made to further improve the performance of these typical solar collectors according to the above results and devote to enhancing the solar penetration in the future energy supply.

CRediT authorship contribution statement

Datong Gao: Conceptualization, Methodology, Software, Validation, Formal analysis, Investigation, Data curation, Writing – original draft, Writing – review & editing, Visualization. **Shuai Zhong:** Conceptualization, Investigation, Data curation. **Xiao Ren:** Methodology, Writing – review & editing. **Trevor Hocksun Kwan:** Writing – review & editing. **Gang Pei:** Conceptualization, Resources, Writing – review & editing, Supervision, Project administration, Funding acquisition.

Declaration of competing interest

The authors declare that they have no known competing financial interests or personal relationships that could have appeared to influence the work reported in this paper.

Acknowledgments

The study was sponsored by the National Natural Science Foundation of China (NSFC 51776193).

Appendix A. Exergy analysis of ETSC and EFPC

For a detailed analysis of the exergy transfer process, we have studied the exergy loss on the ETSC and EFPC. First of all, the exergy equations for both solar collectors can be established (see Table A1). It is noticed that the equations for ETSC are for each tube and the equation for EFPC is for the whole panel.

Table A1
The exergy balance equations of ETSC and EFPC.

Type	ETSC		EFPC	
Equations				
absorber plate	$E_{abs-s} = E_{at-gla} + E_{ad-shd} + E_{abs-pe} + E_{d,abs}$	(11)	$E_{abs-s} = E_{at-gla} + E_{ad-bot} + E_{abs-ht} + E_{d,abs}$	(12)
shield/backplate	$E_{ad-shd} = E_{shd-gla} + E_{d,shd}$	(13)	$E_{ad-bot} = E_{bot-amb}$	(14)
glass tube/plate	$E_{at-gla} + E_{shd-gla} + E_{gla-s} = E_{conv,gla-amb} + E_{r,gla-amb} + E_{d,gla}$	(15)	$E_{at-gla} + E_{gla-s} = E_{conv,gla-amb} + E_{r,gla-amb} + E_{d,gla}$	(16)

In Eq.(11) and (12), $E_{abs\text{-}s}$ is the solar irradiance exergy absorbed by absorber plate:

$$E_{abs-s} = \tau_{gla}\alpha_{abs}GA_{abs}\left(1-\frac{T_{amb}}{T_{abs}}\right) \tag{17}$$

$E_{at\text{-}gla}$ is the solar irradiance exergy transfer from the top of the absorber plate to the glass tube [51]:

$$E_{at-g} = \varepsilon_{at-g}\sigma\left[{T_{abs}}^4 - {T_{gla}}^4 - \frac{4}{3}T_{amb}\left({T_{abs}}^3 - {T_{gla}}^3\right)\right] \tag{18}$$

$$\varepsilon_{at-g} = \frac{1}{\frac{1-\varepsilon_{at}}{\varepsilon_{at}A_{abs}} + \frac{1}{A_{abs}} + \frac{1-\varepsilon_{gla}}{0.5\varepsilon_{gla}A_{gla}}} \tag{19}$$

The coefficient 0.5 in Eq. (19) is caused by A_{gla} is the total area of the glass tube but the heat transfer between absorber plate top side and the glass tube is simplified into only half glass tube joins in this process. Identically, another half glass tube only has thermal radiation with the bottom side of the absorber plate. However, in EFPC, the area of the glass plate is almost the same as the absorber plate, so this coefficient is no need in the EFPC exergy analysis model, i.e. $E_{at,gla}$ in Eq.(12).

In Eq.(11), $E_{ad,shd}$ is the solar irradiance exergy transfer from the bottom of the absorber plate to the shield plate:

$$E_{\mathrm{ad-shd}}=\varepsilon_{\mathrm{ad-shd}}\sigma\left[{T_{\mathrm{amb}}}^4-{T_{\mathrm{shd}}}^4-\frac{4}{3}T_{\mathrm{amb}}\left({T_{\mathrm{abs}}}^3-{T_{\mathrm{shd}}}^3\right)\right] \tag{20}$$

$$\varepsilon_{\mathrm{ad-shd}}=\frac{1}{\frac{1-\varepsilon_{\mathrm{ad}}}{\varepsilon_{\mathrm{ad}}A_{\mathrm{abs}}}+\frac{1}{A_{\mathrm{abs}}}+\frac{1-\varepsilon_{\mathrm{Al}}}{\varepsilon_{\mathrm{Al}}A_{\mathrm{abs}}}} \tag{21}$$

The expression of $E_{\mathrm{ad\text{-}bot}}$ in Eq. (12) is equivalent to $E_{\mathrm{ad\text{-}shd}}$ in Eq.(11).

$E_{\mathrm{abs\text{-}pe}}$ is the exergy transferred from the absorber plate to the heat pipe:

$$E_{\mathrm{abs-pe}}=Q_{\mathrm{abs-pe}}\left(1-\frac{T_{\mathrm{amb}}}{T_{\mathrm{abs}}}\right) \tag{22}$$

$E_{\mathrm{abs\text{-}ht}}$ in Eq. (12)is the same as $E_{\mathrm{abs\text{-}pe}}$ in Eq.(11). $E_{\mathrm{d\text{-}abs}}$ of the absorber plate exergy balance equation can be obtained from Eq. (11) and (12), respectively.

In Eq.(13), $E_{\mathrm{shd\text{-}gla}}$ is the solar irradiance exergy transferred from the bottom of the shield plate to the bottom glass tube:

$$E_{\mathrm{shd-gla}}=\varepsilon_{\mathrm{shd-gla}}\sigma\left[{T_{\mathrm{shd}}}^4-{T_{\mathrm{gla}}}^4-\frac{4}{3}T_{\mathrm{amb}}\left({T_{\mathrm{shd}}}^3-{T_{\mathrm{gla}}}^3\right)\right] \tag{23}$$

where,

$$\varepsilon_{\mathrm{shd-gla}}=\frac{1}{\frac{1-\varepsilon_{\mathrm{Al}}}{\varepsilon_{\mathrm{Al}}A_{\mathrm{abs}}}+\frac{1}{A_{\mathrm{abs}}}+\frac{1-\varepsilon_{\mathrm{gla}}}{0.5\varepsilon_{\mathrm{gla}}A_{\mathrm{gla}}}} \tag{24}$$

$E_{\mathrm{at\text{-}gla}}$ in Eq. (14) is equivalent to $E_{\mathrm{shd\text{-}gla}}$ in Eq.(13), and as aforementioned, the coefficient 0.5Ag should be subscribed with A_{bot} in EFPC exergy analysis. Besides, $E_{\mathrm{d,gla}}$ on the glass cover of both solar collectors can be deduced in Eq. (13)and(14), respectively.

In Eq.(15), $E_{\mathrm{gla\text{-}s}}$ is the solar irradiance exergy absorbed by the glass tube:

$$E_{\mathrm{gla-s}}=\alpha_{\mathrm{gla}}GA_{\mathrm{ga}}\left(1-\frac{T_{\mathrm{amb}}}{T_{\mathrm{gla}}}\right) \tag{25}$$

where A_{ga} is the aperture area of each ETSC tube.

$E_{\mathrm{r,gla\text{-}amb}}$ is the thermal radiation exergy from the glass tube to the surroundings:

$$E_{\mathrm{r,gla-amb}}=\varepsilon_{\mathrm{gla}}A_{\mathrm{gla}}\sigma\left[{T_{\mathrm{gla}}}^4-{T_{\mathrm{amb}}}^4-\frac{4}{3}T_{\mathrm{amb}}\left({T_{\mathrm{gla}}}^3-{T_{\mathrm{amb}}}^3\right)\right] \tag{26}$$

$E_{\mathrm{conv,gla\text{-}amb}}$ is the exergy loss caused by convection heat transfer from the glass tube to the surroundings:

$$E_{\mathrm{conv,gla-amb}}=h_{\mathrm{gla-amb}}A_{\mathrm{gla}}\left(T_{\mathrm{gla}}-T_{\mathrm{amb}}\right)\left(1-\frac{T_{\mathrm{amb}}}{T_{\mathrm{gla}}}\right) \tag{27}$$

The exergy loss caused by optical loss on the gaps between each glass tube:

$$E_{\mathrm{gap}}=GA_{\mathrm{gap}}\psi \tag{28}$$

The exergy loss caused by optical loss on the interval between absorber plate and glass tube:

$$E_{\mathrm{inv}}=\tau_{\mathrm{gla}}\left(GA_{\mathrm{ga}}\psi-GA_{\mathrm{abs}}\psi\right) \tag{29}$$

In Eq.(16), there is an exergy exchange between the bottom side of the absorber plate and the backplate, but this part can be omitted by considering the exergy of the backplate is all lost to the surroundings.

There exists exergy destruction in the solar irradiance exergy transfer to the absorber plate and glass tube/plate. The exergy destruction caused by solar irradiance absorbed by the absorber plate:

$$E_{\mathrm{d,abs}}=\tau_{\mathrm{gla}}GA_{\mathrm{abs}}\psi-E_{\mathrm{abs-s}} \tag{30}$$

The exergy destruction caused by the solar irradiance absorbed by the glass tube:

$$E_{\mathrm{d,gla}}=\left(1-\tau_{\mathrm{gla}}\right)GA_{\mathrm{ga}}\psi-E_{\mathrm{gla-s}} \tag{31}$$

The $E_{\mathrm{w\text{-}ins}}$ denotes the exergy transfer from the HTF to the insulation, and this process only happened in the header tube of ETSC:

$$E_{\mathrm{w-ins}}=\int_{T_i}^{T_e}\left(1-\frac{T_{\mathrm{amb}}}{T_{\mathrm{w}}}\right)dQ_{\mathrm{w-ins}}(T_{\mathrm{w}}) \tag{32}$$

where,

$$\int_{T_i}^{T_e}dQ_{\mathrm{w-ins}}(T_{\mathrm{w}})=(T_{\mathrm{w}}-T_{\mathrm{amb}})U \tag{33}$$

$E_{\mathrm{d,abs\text{-}pc}}$ is the exergy destruction caused by heat transfer from the absorber plate to the heat pipe:

$$E_{\mathrm{d,abs-pc}}=Q_{\mathrm{abs-pe}}\left(\frac{T_{\mathrm{amb}}}{T_{\mathrm{pc}}}-\frac{T_{\mathrm{amb}}}{T_{\mathrm{amb}}}\right) \tag{34}$$

$E_{\mathrm{d,pc\text{-}w}}$ is the exergy destruction caused by the heat transfer from heat pipe to the HTF [65]:

$$E_{\mathrm{d,pc-w}}=T_{\mathrm{amb}}\left[\int_{T_i}^{T_e}\frac{dQ_{\mathrm{pc-w}}(T_{\mathrm{w}})}{T_{\mathrm{w}}}-\frac{1}{T_{\mathrm{pc}}}\int_{T_i}^{T_e}dQ_{\mathrm{pc-w}}(T_{\mathrm{w}})\right] \tag{35}$$

where the i and e are referred to as inlet and outlet, T_{w} is the temperature of the HTF in the header pipe, and

$$\int_{T_i}^{T_e}dQ_{\mathrm{pc-w}}(T_{\mathrm{w}})=Q_{\mathrm{abs,pe}} \tag{36}$$

Additionally, the HTF flow in the pipes will lead to exergy loss due to friction. However, it can be omitted since it only accounts for a tiny amount compared with the total exergy loss [66].

Appendix B. Energy analysis model

The detailed numerical model for EFPC is established as follows. Considering the inhomogeneity temperature distribution, a mesh is implemented on the absorber plate and heat pipes. Other parts like the glass cover and bottom plate are considered as the uniform temperature on the steady-state.

The energy balance equation of glass cover is:

$$\begin{aligned}\alpha_{\mathrm{gla}}A_{\mathrm{gla}}G+Q_{\mathrm{r,abs-gla}}&=A_{\mathrm{gla}}\varepsilon_{\mathrm{gla}}\sigma\left(T_{\mathrm{gla}}^4-T_{\mathrm{sky,eq}}^4\right)\\&\quad+A_{\mathrm{gla}}h_{\mathrm{gla-amb}}\left(T_{\mathrm{gla}}-T_{\mathrm{amb}}\right)\end{aligned} \tag{37}$$

where,

$$Q_{r,abs-gla} = \sum_{m,n=1}^{m=M,n=N} \varepsilon_{at} \Delta A_{abs(m,n)} \sigma \left(T_{abs(m,n)}^4 - T_{gla}^4 \right) \tag{38}$$

and $T_{sky,eq}$ is the equivalent temperature of the sky.
The energy equation of the absorber plate is:

$$\tau_{gla} \alpha_{abs} A_{abs} G = Q_{r,abs-gla} + Q_{r,abs-bot} + Q_{abs-ht} \tag{39}$$

where,

$$Q_{r,abs-bot} = \sum_{m,n=1}^{m=M,n=N} \varepsilon_{ad} \Delta A_{abs(m,n)} \sigma \left(T_{abs(m,n)}^4 - T_{bot}^4 \right) \tag{40}$$

$$Q_{abs-ht} = \frac{(T_{abs}(m,n) - T_{ht}(m))}{R_{abs-ht}} \tag{41}$$

The energy equation of each mesh on heat tubes is:

$$\begin{aligned} Q_{abs-ht} + k_{ht} A_{ht} \frac{T_{ht}(m+1) - 2T_{ht}(m) + T_{ht}(m-1)}{\Delta x_{ht}} \\ = Q_{r,ht-bot} + \frac{(T_{ht}(m) - \overline{T}_w(m))}{R_{ht-w}} \end{aligned} \tag{42}$$

The energy equation of each mesh on HTF is:

$$\frac{(T_{ht}(m) - \overline{T}_w(m))}{R_{ht-w}} = \dot{m}_w c_w \left(T_{w,out}(m) - T_{w,in}(m) \right) \tag{43}$$

The main calculation targets are the glass cover temperature, the absorber plate's temperature, heat tubes' temperature, bottom plate's temperature, and outlet temperature of HTF. The thermal properties of all materials used in this model are the same as the real solar collector. An iteration calculation was carried out until the values have reached convergence. The detailed energy efficiency analysis model of ETSC can be found in the previous study [54]. Different mesh quantities are tested to examine the accuracy of the model. Under the same boundary conditions (the solar irradiance is 800 W/m^2, the flow rate is 0.03 kg/s, the ambient temperature is 25 °C, the inlet temperature is 100 °C, and the wind velocity is 2 m/s). As shown in Fig. 17, the thermal efficiency is not sensitive to the mesh quantity after it exceeds 1000. Considering that the computing resource, mesh quantity of 1260 is applied for this study.

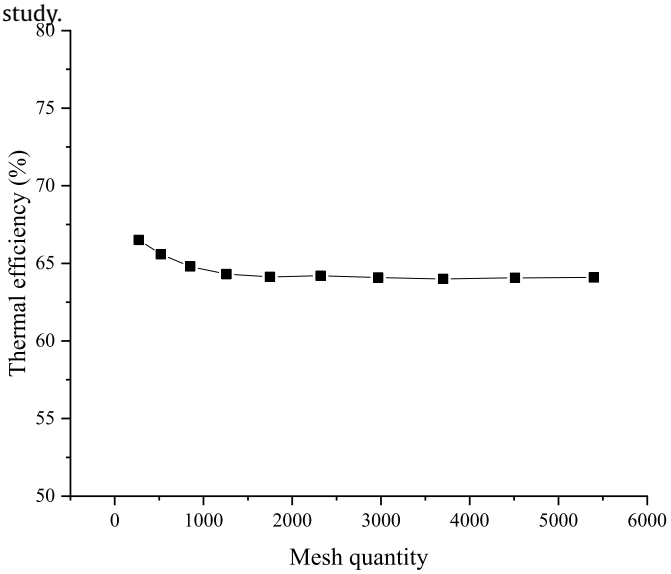

Fig. 17. Variation of the thermal efficiency as the change of mesh quantity.

Appendix C. Thermal resistance analysis

The thermal resistance of each energy transfer process for two solar collectors is studied. The main heat transfer processes in the solar collector are the heat radiant among absorber plate, glass cover, ETSC. For comparison, the original structure, i.e., the ETSC without heat shield plate and flat plate solar collector, is also incorporated in this analysis. Each thermal resistance term of ETSC and flat plate solar collector is defined in Table A2 and Table A3.
where,

$$h_{r,gla-sky} = \frac{\varepsilon_{gla} \sigma \left(T_{gla}^4 - T_{sky,eq}^4 \right)}{(T_{abs} - T_{amb})} \tag{49}$$

$$h_{conv,gla-amb} = 5.7 + 3.8 v_{wind} \tag{50}$$

$$h_{r,gla-abs} = \frac{\sigma \left(T_{abs}^2 + T_{gla}^2 \right) \left(T_{abs} + T_{gla} \right)}{\frac{1-\varepsilon_{at}}{\varepsilon_{abst}} + 1 + \frac{(1-\varepsilon_{gla}) A_{abs}}{0.5 \varepsilon_{gla} A_{gla}}} \tag{51}$$

$$h_{r,abs-shd} = \frac{\sigma \left(T_{abs}^2 + T_{shd}^2 \right) (T_{abs} + T_{shd})}{\frac{1}{\varepsilon_{ad}} + \frac{1}{\varepsilon_{shd}} - 1} \tag{52}$$

$$h_{r,shd-gla} = \frac{\sigma \left(T_{shd}^2 + T_{gla}^2 \right) \left(T_{shd} + T_{gla} \right)}{\frac{1-\varepsilon_{shd}}{\varepsilon_{shd}} + 1 + \frac{(1-\varepsilon_{gla}) A_{shd}}{0.5 \varepsilon_{gla} A_{gla}}} \tag{53}$$

$$h_{r,gla-grd} = \frac{\sigma \left(T_{grd}^2 + T_{gla}^2 \right) \left(T_{grd} + T_{gla} \right)}{\frac{1}{\varepsilon_{shd}} + \frac{1}{\varepsilon_{grd}} - 1} \tag{54}$$

The bottom side of the absorber plate will have direct radiation with the glass tube if there is no shield plate in ETSC. Hence, Eqs. (46) and (47) should be combined in the original structure calculation. The thermal resistances of flat plate solar collector are presented in Table A3. For the EFPC analysis, the internal convection heat transfer between the absorber plate, bottom plate, and glass plate is deemed as nonexistent. Thus, the convection terms in Eqs. (56) and (57) should be omitted.
where,

$$h_{r,gla-sky} = \frac{\varepsilon_{gla} \sigma \left(T_{gla}^4 - T_{sky,eq}^4 \right)}{(T_{abs} - T_{amb})} \tag{59}$$

$$h_{conv,gla-amb} = 5.7 + 3.8 v_{wind} \tag{60}$$

$$h_{r,gla-abs} = \frac{\sigma \left(T_{abs}^2 + T_{gla}^2 \right) \left(T_{abs} + T_{gla} \right)}{\frac{1}{\varepsilon_{at}} + \frac{1}{\varepsilon_{gla}} - 1} \tag{61}$$

$$h_{conv,gla-abs} = Nu \frac{\lambda_{air}}{d_{gla-abs}} \tag{62}$$

$$\begin{aligned} Nu = 1 + 1.14 \left(1 - \frac{1708 (\sin 1.8\,\beta)^{1.6}}{Ra \cdot \cos \beta} \right) \left[1 - \frac{1708}{Ra \cdot \cos \beta} \right]^+ \\ + \left[\left(\frac{Ra \cdot \cos \beta}{5830} \right)^{1/3} - 1 \right]^+ \end{aligned} \tag{63}$$

Table A2
The thermal resistance expression of ETSC.

Term	Thermal resistance	
Heat transfer between the glass tube and sky	$R_{\mathrm{gla-sky}} = 1/\left(1/\frac{1}{h_{\mathrm{conv,gla-sky}}} + 1/\frac{1}{h_{\mathrm{r,gla-sky}}}\right) = \frac{1}{h_{\mathrm{conv,gla-sky}} + h_{\mathrm{r,gla-sky}}}$	(44)
Heat transfer between the glass tube and absorber plate	$R_{\mathrm{gla-abs}} = \frac{1}{h_{\mathrm{r,gla-abs}}}$	(45)
Heat transfer between the absorber plate and shield plate	$R_{\mathrm{abs-shd}} = \frac{1}{h_{\mathrm{r,abs-shd}}}$	(46)
Heat transfer between the shield plate and glass tube	$R_{\mathrm{shd-gla}} = \frac{1}{h_{\mathrm{r,shd-gla}}}$	(47)
Heat transfer between the glass tube and ambient environment	$R_{\mathrm{gla-amb}} = 1/\left(1/\frac{1}{h_{\mathrm{conv,gla-amb}}} + 1/\frac{1}{h_{\mathrm{r,gla-grd}}}\right) = \frac{1}{h_{\mathrm{conv,gla-amb}} + h_{\mathrm{r,gla-grd}}}$	(48)

Table A3
The thermal resistance expression of flat plate solar collector.

Term	Thermal resistance	
Heat transfer between the glass plate and sky	$R_{\mathrm{gla-sky}} = 1/\left(1/\frac{1}{h_{\mathrm{conv,gla-sky}}} + 1/\frac{1}{h_{\mathrm{r,gla-sky}}}\right) = \frac{1}{h_{\mathrm{conv,gla-sky}} + h_{\mathrm{r,gla-sky}}}$	(55)
Heat transfer between the glass plate and absorber plate	$R_{\mathrm{gla-abs}} = 1/\left(1/\frac{1}{h_{\mathrm{conv,gla-abs}}} + 1/\frac{1}{h_{\mathrm{r,gla-abs}}}\right) = \frac{1}{h_{\mathrm{conv,gla-abs}} + h_{\mathrm{r,gla-abs}}}$	(56)
Heat transfer between the absorber plate and bottom plate	$R_{\mathrm{abs-bot}} = 1/\left(1/\frac{1}{h_{\mathrm{cond,abs-bot}}} + 1/\frac{1}{h_{\mathrm{r,abs-bot}}}\right) = \frac{1}{h_{\mathrm{cond,abs-bot}} + h_{\mathrm{r,abs-bot}}}$	(57)
Heat transfer between the bottom plate and ambient environment	$R_{\mathrm{bot-amb}} = 1/\left(1/\frac{1}{h_{\mathrm{conv,bot-amb}}} + 1/\frac{1}{h_{\mathrm{r,bot-grd}}}\right) = \frac{1}{h_{\mathrm{conv,bot-amb}} + h_{\mathrm{r,bot-grd}}}$	(58)

$$Ra = \frac{g\beta' \Delta T L^3}{\nu\alpha} \tag{64}$$

$$h_{\mathrm{r,abs-bot}} = \frac{\sigma\left(T_{\mathrm{abs}}^2 + T_{\mathrm{bot}}^2\right)\left(T_{\mathrm{abs}} + T_{\mathrm{bot}}\right)}{\frac{1}{\varepsilon_{\mathrm{ad}}} + \frac{1}{\varepsilon_{\mathrm{bot}}} - 1} \tag{65}$$

$$h_{\mathrm{cond,abs-bot}} = \frac{\lambda_{\mathrm{ins}}}{d_{\mathrm{abs-bot}}} \tag{66}$$

$$h_{\mathrm{conv,bot-amb}} = 5.7 + 3.8 v_{\mathrm{wind}} \tag{67}$$

$$h_{\mathrm{r,bot-grd}} = \frac{\sigma\left(T_{\mathrm{bot}}^2 + T_{\mathrm{grd}}^2\right)\left(T_{\mathrm{bot}} + T_{\mathrm{grd}}\right)}{\frac{1}{\varepsilon_{\mathrm{bot}}} + \frac{1}{\varepsilon_{\mathrm{grd}}} - 1} \tag{68}$$

Appendix D. Advanced exergy analysis

For k_{th} component in the solar collector, the exergy fuel flow for itself can be divided into the product part for the next component and the destruction part [67]:

$$E_{\mathrm{fuel}}^{k} = E_{\mathrm{prod}}^{k} + E_{\mathrm{dst}}^{k} \tag{69}$$

The unavoidable exergy destruction is defined as [68]:

$$E_{\mathrm{dst},k}^{\mathrm{UN}} = E_{prod,k}^{\mathrm{real}} \left(\frac{E_{\mathrm{dst}}}{E_{\mathrm{prod}}}\right)_{k}^{\mathrm{hypo}} \tag{70}$$

where the k_{th} component works in its hypothetical condition while the other components work at their real conditions.

The avoidable exergy destruction is defined as [60]:

$$E_{\mathrm{dst},k}^{\mathrm{AVO}} = E_{\mathrm{dst},k}^{\mathrm{real}} - E_{\mathrm{dst},k}^{\mathrm{UN}} \tag{71}$$

References

[1] B. Dudley, BP Statistical Review of World Energy, BP Statistical Review, London, UK, 2018. (Accessed 6 August 2018).
[2] M.S. Guney, Solar power and application methods, Renew. Sustain. Energy Rev. 57 (2016) 776–785.
[3] O. Behar, D. Sbarbaro, L. Moran, A practical methodology for the design and cost estimation of solar tower power plants, Sustainability-Basel 12 (20) (2020).
[4] A.A.A. Arani, F. Monfaredi, Energy and exergy analyses of nanofluid-filled parabolic trough solar collector with acentric absorber tube and insulator roof, J. Therm. Anal. Calorim. 145 (2021) 787–816.
[5] M. Palacio, A. Rincon, M. Carmona, Experimental comparative analysis of a flat plate solar collector with and without PCM, Sol. Energy 206 (2020) 708–721.
[6] G. Sadeghi, M. Najafzadeh, M. Ameri, Thermal characteristics of evacuated tube solar collectors with coil inside: an experimental study and evolutionary algorithms, Renew. Energy 151 (2020) 575–588.
[7] E. Keyif, M. Hornung, W.S. Zhu, Optimal configurations and operations of concentrating solar power plants under new market trends, Appl. Energy 270 (2020).
[8] G.K. Manikandan, S. Iniyan, R. Goic, Enhancing the optical and thermal efficiency of a parabolic trough collector - a review, Appl. Energy 235 (2019) 1524–1540.
[9] C. Garnier, T. Muneer, J. Currie, Numerical and empirical evaluation of a novel building integrated collector storage solar water heater, Renew. Energy 126 (2018) 281–295.
[10] Z.Y. Tian, B. Perers, S. Furbo, J.H. Fan, Thermo-economic optimization of a hybrid solar district heating plant with flat plate collectors and parabolic trough collectors in series, Energy Convers. Manag. 165 (2018) 92–101.
[11] B. Widyolar, L. Jiang, J. Ferry, R. Winston, Non-tracking East-West XCPC solar thermal collector for 200 celsius applications, Appl. Energy 216 (2018) 521–533.
[12] Z. Said, R. Saidur, N.A. Rahim, Energy and exergy analysis of a flat plate solar collector using different sizes of aluminium oxide based nanofluid, J. Clean. Prod. 133 (2016) 518–530.
[13] N. Hartmann, C. Glueck, F.P. Schmidt, Solar cooling for small office buildings: comparison of solar thermal and photovoltaic options for two different European climates, Renew. Energy 36 (5) (2011) 1329–1338.
[14] L. Zhao, B. Bhatia, S. Yang, E. Strobach, L.A. Weinstein, T.A. Cooper, G. Chen, E.N. Wang, Harnessing heat beyond 200 degrees C from unconcentrated

sunlight with nonevacuated transparent aerogels, ACS Nano 13 (7) (2019) 7508–7516.
[15] A. Vandermeulen, B. van der Heijde, L. Helsen, Controlling district heating and cooling networks to unlock flexibility: a review, Energy 151 (2018) 103–115.
[16] A. Alahmer, X.L. Wang, R. Al-Rbaihat, K.C.A. Alam, B.B. Saha, Performance evaluation of a solar adsorption chiller under different climatic conditions, Appl. Energy 175 (2016) 293–304.
[17] C. Liu, W. Han, Z. Wang, N. Zhang, Q. Kang, M. Liu, Proposal and assessment of a new solar space heating system by integrating an absorption-compression heat pump, Appl. Energy 294 (2021), 116966.
[18] L. Zhao, B. Bhatia, L.N. Zhang, E. Strobach, A. Leroy, M.K. Yadav, S. Yang, T.A. Cooper, L.A. Weinstein, A. Modi, S.B. Kedare, G. Chen, E.N. Wang, A passive high-temperature high-pressure solar steam generator for medical sterilization, Joule 4 (12) (2020) 2733–2745.
[19] M.B. Elsheniti, A. Kotb, O. Elsamni, Thermal performance of a heat-pipe evacuated-tube solar collector at high inlet temperatures, Appl. Therm. Eng. 154 (2019) 315–325.
[20] P.H. Federico Giovannetti, Comparison of Process Heat Collectors with Respect to Technical and Economic Conditions, 2016.
[21] G. Sadeghi, S. Nazari, M. Ameri, F. Shama, Energy and exergy evaluation of the evacuated tube solar collector using Cu2O/water nanofluid utilizing ANN methods, Sustain. Energy Technol. Assess. 37 (2020).
[22] K. Morawietz, M. Hermann, Integrated development and modeling of heat pipe solar collectors, Energy Procedia 48 (2014) 157–162.
[23] K. Anirudh, S. Dhinakaran, Numerical study on performance improvement of a flat-plate solar collector filled with porous foam, Renew. Energy 147 (2020) 1704–1717.
[24] D.N. Nkwetta, M. Smyth, Performance analysis and comparison of concentrated evacuated tube heat pipe solar collectors, Appl. Energy 98 (2012) 22–32.
[25] D.N. Nkwetta, M. Smyth, A. Zacharopoulos, T. Hyde, Optical evaluation and analysis of an internal low-concentrated evacuated tube heat pipe solar collector for powering solar air-conditioning systems, Renew. Energy 39 (1) (2012) 65–70.
[26] J. Vestlund, M. Ronnelid, J.O. Dalenback, Thermal performance of gas-filled flat plate solar collectors, Sol. Energy 83 (6) (2009) 896–904.
[27] N. Benz, T. Beikircher, High efficiency evacuated flat-plate solar collector for process steam production, Sol. Energy 65 (2) (1999) 111–118.
[28] R.W. Moss, G.S.F. Shire, P. Henshall, P.C. Eames, F. Arya, T. Hyde, Design and fabrication of a hydroformed absorber for an evacuated flat plate solar collector, Appl. Therm. Eng. 138 (2018) 456–464.
[29] R.W. Moss, P. Henshall, F. Arya, G.S.F. Shire, P.C. Eames, T. Hyde, Simulator testing of evacuated flat plate solar collectors for industrial heat and building integration, Sol. Energy 164 (2018) 109–118.
[30] R. Moss, S. Shire, P. Henshall, F. Arya, P. Eames, T. Hyde, Performance of evacuated flat plate solar thermal collectors, Therm. Sci. Eng. Prog. 8 (2018) 296–306.
[31] F. Calise, M.D. d'Accadia, M. Vicidomini, M. Scarpellino, Design and simulation of a prototype of a small-scale solar CHP system based on evacuated flat-plate solar collectors and Organic Rankine Cycle, Energy Convers. Manag. 90 (2015) 347–363.
[32] A.A. Gunay, H. Kim, N. Nagarajan, M. Lopez, R. Kantharaj, A. Alsaati, A. Marconnet, A. Lenert, N. Miljkovic, Optically transparent thermally insulating silica aerogels for solar thermal insulation, ACS Appl. Mater. Int. 10 (15) (2018) 12603–12611.
[33] Y. Fu, G. Wang, T. Mei, J.H. Li, J.Y. Wang, X.B. Wang, Accessible graphene aerogel for efficiently harvesting solar energy, ACS Sustain. Chem. Eng. 5 (6) (2017) 4665–4671.
[34] Z.J. Berquist, K.K. Turaczy, A. Lenert, Plasmon-enhanced greenhouse selectivity for high-temperature solar thermal energy conversion, ACS Nano 14 (10) (2020) 12605–12613.
[35] B. Mosavati, M. Mosavati, A new approach to solve inverse boundary design of a radiative enclosure with specular-diffuse surfaces, J. Heat Tran. (2021).
[36] B. Mosavati, M. Mosavati, F. Kowsary, Inverse boundary design solution in a combined radiating-free convecting furnace filled with participating medium containing specularly reflecting walls, Int. Commun. Heat Mass 76 (2016) 69–76.
[37] P. Olczak, D. Matuszewska, J. Zabaglo, The comparison of solar energy gaining effectiveness between flat plate collectors and evacuated tube collectors with heat pipe: case study, Energies 13 (7) (2020).
[38] L.M. Ayompe, A. Duffy, M. Mc Keever, M. Conlon, S.J. McCormack, Comparative field performance study of flat plate and heat pipe evacuated tube collectors (ETCs) for domestic water heating systems in a temperate climate, Energy 36 (5) (2011) 3370–3378.
[39] M. Moldovan, I. Visa, B.G. Burduhos, Experimental comparison of flat plate and evacuated tube solar thermal collectors for domestic hot water preparation in education facilities, J. Sustain. Dev. Energy 8 (2) (2020) 293–303.
[40] M. Eltaweel, A.A. Abdel-Rehim, A.A.A. Attia, A comparison between flat-plate and evacuated tube solar collectors in terms of energy and exergy analysis by using nanofluid, Appl. Therm. Eng. 186 (2021).
[41] T. Sokhansefat, A. Kasaeian, K. Rahmani, A.H. Heidari, F. Aghakhani, O. Mahian, Thermoeconomic and environmental analysis of solar flat plate and evacuated tube collectors in cold climatic conditions, Renew. Energy 115 (2018) 501–508.
[42] R. Hoffmann, M. Brondani, F. Pappis, A. Friderichs, S. Serafini, E.L. Foletto, Economic-environmental comparison between flat plate and evacuated tube solar collectors, Glob. Nest J. 16 (6) (2014) 1100–1109.
[43] H.G. Ozcan, S. Varga, H. Gunerhan, A. Hepbasli, Numerical and experimental work to assess dynamic advanced exergy performance of an on-grid solar photovoltaic-air source heat pump-battery system, Energy Convers. Manag. 227 (2021).
[44] TVP Solar, 2021. www.tvpsolar.com.
[45] S.A.o. China, Test Method for Thermal Performance of Solar Collectors, 2007.
[46] L.S. Sundar, M.K. Singh, V. Punnaiah, A.C.M. Sousa, Experimental investigation of Al2O3/water nanofluids on the effectiveness of solar flat-plate collectors with and without twisted tape inserts, Renew. Energy 119 (2018) 820–833.
[47] M.A. Sharafeldin, G. Grof, O. Mahian, Experimental study on the performance of a flat-plate collector using WO3/Water nanofluids, Energy 141 (2017) 2436–2444.
[48] M.A. Sharafeldin, G. Grof, Experimental investigation of flat plate solar collector using CeO2-water nanofluid, Energy Convers. Manag. 155 (2018) 32–41.
[49] Y.J. Tong, H. Lee, W. Kan, H. Cho, Energy and exergy comparison of a flat-plate solar collector using water, Al2O3 nanofluid, and CuO nanofluid, Appl. Therm. Eng. 159 (2019).
[50] S. Abo-Elfadl, H. Hassan, M.F. El-Dosoky, Energy and exergy assessment of integrating reflectors on thermal energy storage of evacuated tube solar collector-heat pipe system, Sol. Energy 209 (2020) 470–484.
[51] R. Petela, Exergy of undiluted thermal radiation, Sol. Energy 74 (6) (2003) 469–488.
[52] A. Shafieian, M. Khiadani, A. Nosrati, Thermal performance of an evacuated tube heat pipe solar water heating system in cold season, Appl. Therm. Eng. 149 (2019) 644–657.
[53] A.A.B. Baloch, H.M.S. Bahaidarah, P. Gandhidasan, F.A. Al-Sulaiman, Experimental and numerical performance analysis of a converging channel heat exchanger for PV cooling, Energy Convers. Manag. 103 (2015) 14–27.
[54] X.N. Huang, Q.L. Wang, H.L. Yang, S. Zhong, D.S. Jiao, K.L. Zhang, M.J. Li, G. Pei, Theoretical and experimental studies of impacts of heat shields on heat pipe evacuated tube solar collector, Renew. Energy 138 (2019) 999–1009.
[55] K. Mohamad, P. Ferrer, Parabolic trough efficiency gain through use of a cavity absorber with a hot mirror, Appl. Energy 238 (2019) 1250–1257.
[56] Y. Qiu, Y.C. Xu, Q. Li, J.K. Wang, Q.L. Wang, B. Liu, Efficiency enhancement of a solar trough collector by combining solar and hot mirrors, Appl. Energy 299 (2021).
[57] C. D'Alessandro, D. De Maio, M. Musto, D. De Luca, E. Di Gennaro, P. Bermel, R. Russo, Performance analysis of evacuated solar thermal panels with an infrared mirror, Appl. Energy 288 (2021), 116603.
[58] V. Badescu, How much work can be extracted from diluted solar radiation? Sol. Energy 170 (2018) 1095–1100.
[59] Y.D. Kim, J.H. Shin, J.Y. Cho, H.J. Choi, H. Lee, Nanosized patterned protective glass exhibiting high transmittance and self-cleaning effects for photovoltaic systems, Phys. Status Solidi 211 (8) (2014) 1822–1827.
[60] A. Mortazavi, M. Ameri, Conventional and advanced exergy analysis of solar flat plate air collectors, Energy 142 (2018) 277–288.
[61] B. Liu, C.Y. Wang, S. Bazri, I.A. Badruddin, Y. Orooji, S. Saeidi, S. Wongwises, O. Mahian, Optical properties and thermal stability evaluation of solar absorbers enhanced by nanostructured selective coating films, Powder Technol. 377 (2021) 939–957.
[62] X.H. Zheng, X. Yang, J.P. Wan, T. Zhang, Z. Yang, L. Wang, H.S. Chen, F.X. Liang, D.W. Tang, A novel super thermal insulation material: bamboo-like polymer nanotubes, Nanotechnology 31 (34) (2020).
[63] V. Selvaraj, H. Krishnan, Synthesis of graphene encased alumina and its application as nanofluid for cooling of heat-generating electronic devices, Powder Technol. 363 (2020) 665–675.
[64] T.P. Teng, T.C. Hsiao, C.C. Chung, Characteristics of carbon-based nanofluids and their application in a brazed plate heat exchanger under laminar flow, Appl. Therm. Eng. 146 (2019) 160–168.
[65] A. Suzuki, General-theory of exergy-balance analysis and application to solar collectors, Energy 13 (2) (1988) 153–160.
[66] R.V. Padilla, A. Fontalvo, G. Demirkaya, A. Martinez, A.G. Quiroga, Exergy analysis of parabolic trough solar receiver, Appl. Therm. Eng. 67 (1–2) (2014) 579–586.
[67] S. Kelly, G. Tsatsaronis, T. Morosuk, Advanced exergetic analysis: approaches for splitting the exergy destruction into endogenous and exogenous parts, Energy 34 (3) (2009) 384–391.
[68] F. Cziesla, G. Tsatsaronis, Z.L. Gao, Avoidable thermodynamic inefficiencies and costs in an externally fired combined cycle power plant, Energy 31 (10–11) (2006) 1472–1489.